



PRediction Of Geospace Radiation Environment and Solar wind parameterS

Work Package 4
Development of new statistical wave models
and the re-estimation of the quasilinear
diffusion coefficients.

Deliverable 4.4
Final version of the statistical wave models

Vitalii Shastun, Vladimir Krasnoselskikh, Oleksiy Agapitov,
Michael Balikhin, Simon Walker, Richard Boyton

December 25th, 2016

This project has received funding from the *European Unions Horizon 2020 research and innovation programme* under grant agreement No 637302.



Document Change Record

Issue	Date	Author	Details
1.0	02.12.2016	V. Shastun	Initial draft
2.0	23.12.2016	V. Shastun	Added simplified model on K_P
3.0	08.02.2018	S. Walker	Updates resulting from third review.

Contents

1	Introduction	5
2	Data description	9
3	Methodology	12
4	Analysis results	13
4.1	LBC wave models	14
4.2	Hiss wave models	17
4.3	EMW wave models	18
4.4	Models of simplified dependence on K_P	20
4.5	Hiss intensity latitudinal extent	24
5	Database description	30
6	Conclusions	30
A	LBC models	39

B Hiss models	46
C EMW models	56
D Models with simplified dependence on K_P	63
E Examples	67
E.1 Python	67
E.2 MATLAB	67

Summary

The deliverable D4.4 entitled "Final version of the statistical wave models" is the fourth deliverable of WP4 "Development of the new statistical wave models and the re-estimation of quasilinear diffusion coefficients". The main goal of this WP is to redevelop statistical wave models for whistler mode Chorus, hiss and equatorial magnetosonic waves, that are parameterized by geomagnetic indices (K_p , Dst , A_E), solar wind velocity, density, and interplanetary magnetic field (IMF) and accounts for the previous evolution of these parameters.

Work Package 4 is dedicated to the development of advanced statistical wave models, which can be used to calculate the quasi-linear diffusion coefficients within the radiation belts. Presently, the statistical models of such waves as lower band chorus (LBC), hiss, and equatorial magnetosonic waves (EMW), are parameterised by the location and geomagnetic activity indices. Therefore, prior evolution of the magnetosphere is not taken into account in such models. However, there is no experimental basis to assume that the spatial wave distribution is independent of the current phase of the particular storm. Also, it is known that electron fluxes at GEO are influenced more by solar wind parameters. Hence, previous states of the magnetosphere should be taken into account in the final wave distribution models. New statistical wave models must depend on the parameters that are statistically related to the fluxes of electrons in the radiation belts.

The main goal of this deliverable is to develop analytical models of VLF/ELF emissions as functions of the geomagnetic activity indices and solar wind parameters that influence on different emissions within the inner magnetosphere. The emissions that we are concerned with for this study are LBC, hiss, and EMW. For this deliverable two spacecraft missions were selected (Cluster, THEMIS), which covered most of the key regions of the magnetosphere: the dayside magnetospheric boundary, both at mid-latitudes and in the cusp, the near-Earth magnetospheric tail. Our specific goal was to study properties of VLF/ELF emissions in the Earth magnetosphere, perform a reconstruction of

the emissions' distribution in the radiation belts. To achieve this aim the data from the magnetic field measurements registered onboard of the selected spacecraft missions was used to determine the major characteristics of VLF/ELF emissions around the equator region, namely, wave amplitudes and wave occurrence rate for different geomagnetic activity conditions. We performed automatic detection of LBC, hiss, and EMW to identify occurrences and amplitudes of the corresponding emissions. New statistical wave models were developed based on the final set of parameters and time lags identified by ERR from deliverable 4.3 for the wave amplitudes of LBC, hiss, and EMW.

1 Introduction

Today satellites are widely used in many fields including communications, global positioning, meteorology, science, security, etc. During last five years the number of operational satellites increased considerably from approximately 981 satellites in 2011 to 1381 satellites in 2016 (SIA, 2016). Such a rapid growth show the importance of space industry for the modern world and its dependence on satellite services.

Satellites carrying expensive electronic equipment are very susceptible to variations in space weather. Energetic particles that expose the threat to satellite equipment are trapped inside Van Allen radiation belts – two regions encircling the Earth whose dynamics is controlled by solar activity. These particles can penetrate electronic components causing noise increase, additional power consumption or even electrostatic discharge and complete component failure. During the Halloween solar storm that occurred from mid-October to early November 2003, 47 satellites reported malfunctions (Horne *et al.*, 2013) that are believed to be connected with large changes in radiation belts. Therefore forecasting and warning of the space radiation environment is one of the major tasks for the geophysics community.

The Van Allen radiation belt particle populations exist in a dynamic equilibrium between losses (mainly due to particle precipitation to the upper atmosphere) and re-

filling due to external injections, transport, and acceleration processes. The recent results from the Van Allen Probes support the local nature of particle acceleration (Reeves *et al.*, 2013), and it is now generally agreed that in-situ acceleration (and scattering) mechanisms are important to the outer radiation belt particles dynamics.

VLF/ELF waves have shown to play a significant role in the evolution of high-energy particle fluxes inside the radiation belts. Different approaches are used for the description of the scattering, trapping, and acceleration of charged particles in radiation belts. Favoured mechanisms for driving in-situ acceleration (as well as pitch angle scattering) are the interaction of electrons with whistler waves (chorus and hiss) (Horne *et al.*, 2005b; Thorne *et al.*, 2013), EMIC waves (Blum *et al.*, 2016; Usanova *et al.*, 2014), magnetosonic waves (Mourenas *et al.*, 2013), and nonlinear time domain structures (TDS) (Mozer *et al.*, 2014, 2015). Since the maximum of chorus wave amplitudes is observed inside the outer Van Allen radiation belt and the frequency is close to ω_{ce} , these waves are supposed to be one of the key factors that affect the dynamics of the outer radiation belt (Agapitov *et al.*, 2013; Horne *et al.*, 2005a; Thorne, 2010).

Several forecast models developed by (Balikhin *et al.*, 2011; Boynton *et al.*, 2013; Kellerman *et al.*, 2013) to predict relativistic electron fluxes on geosynchronous orbit are based upon solar wind parameters using nonlinear/correlation analysis. While physics-based models are based on assumption that wave-particles interactions are well described by quasi-linear theory (Kennel and Petschek, 1966; Trakhtengerts, 1966), this theory is applicable for waves with small amplitudes and wide spectrum that allows to consider wave-particle interactions as a random process characterised by a relatively slow scattering of particles in velocity space.

A favourable approach for the calculation of dynamics of relativistic particles population is based on the incorporation of pitch-angle and energy diffusion coefficients into the Fokker-Plank equation. Glauert and Horne (2005) developed computer code that calculates fully relativistic quasi-linear diffusion coefficients that can be applied to any ratio

of ω_{pe}/ω_{ce} (where ω_{pe} and ω_{ce} are plasma and cyclotron frequencies respectively). Simplified code that takes into account interactions of electrons only with parallel whistler waves, but allows to calculate the diffusion coefficients dynamically, was presented by (Shprits *et al.*, 2006). Albert (2007, 2008) proposed approximations that allow replacing the integration over the wave-normal distribution by an evaluation at attentively chosen points. Theoretical study of diffusion coefficients that accounts for both the integration over the wave-normal distribution and the summation over all the relevant n-harmonic resonances were made in works (Mourenas and Ripoll, 2012; Mourenas *et al.*, 2012). All these approaches rely on several models of the background magnetospheric environment and the main properties of the VLF/ELF wave spectrum.

VLF/ELF are typically separated by their frequency on upper band chorus waves with $0.5\omega_{ce0} < \omega < \omega_{ce0}$, lower band chorus waves with $0.1\omega_{ce0} < \omega < 0.5\omega_{ce0}$, hiss waves with $\omega_{LH} < \omega < 0.1\omega_{ce0}$, and below $\omega_{LH} \sim (m_e/m_i)1/2\omega_{ce0}$ (Li *et al.*, 2013; Meredith *et al.*, 2004) (where m_e/m_i is the ratio of the electron mass to the effective mass of ions), ion cyclotron waves with frequency around of gyrofrequencies of oxygen, helium, and hydrogen.

Lower band chorus waves as the most intense emissions in the outer radiation belt are responsible for some of the most effective wave-particle interactions (Thorne *et al.*, 2013). Chorus waves are right-hand polarised coherent waves, that appear as discrete elements of rising or falling tones in frequency-time diagrams (see, e.g., Agapitov *et al.*, 2010, 2011; Helliwell, 1965, and references therein). These emissions are observed predominantly near and outside the outer boundary of the plasmasphere (Gurnett and Inan, 1988; Koons and Roeder, 1990; Sazhin and Hayakawa, 1992; Tsurutani and Smith, 1974). Chorus waves occur typically from 00:00 to 15:00 MLT, but mostly between 06:00 and 12:00 MLTs (Koons and Roeder, 1990; Tsurutani and Smith, 1974). Main properties of chorus waves were studied by making use of the measurements obtained on the board of the Dynamics Explorer 1 (André *et al.*, 2002), CRRES (Meredith *et al.*, 2001, 2004), Cluster (Agapitov

et al., 2011; Agapitov *et al.*, 2011; Pokhotelov *et al.*, 2008), and Thermal Emission Imaging System (THEMIS) (Cully *et al.*, 2008; Li *et al.*, 2011) spacecraft. It was shown that wave intensity B_w^2 strongly depends on the wave frequency range, L shell, magnetic latitude, magnetic local time (MLT), and geomagnetic activity. This dependence was approximated in many studies by different models: stepwise functions were used by Horne *et al.* (2005a) and Ni *et al.* (2011), polynomial fitting up to $\lambda < 15^\circ$ was provided by Spasojevic and Shprits (2013), and a polynomial fitting over a wide λ range for several fixed levels of geomagnetic activity was described by Artemyev *et al.* (2012) and Mourenas *et al.* (2014). Since mentioned models are parameterized by the location of observations and current values of geomagnetic indices the former state of the magnetosphere plays no role in the current wave distribution in the magnetosphere.

In this deliverable we analyse data registered by Cluster and THEMIS missions between 2007 and 2014 to develop new and more comprehensive empirical models of VLF/ELF emissions in equatorial region $|\lambda| < 20^\circ$ at radial distances from 4 to 7 R_E as a function of control parameters listed in table 1. These parameters were identified by ERR analysis as the solar wind parameters and geomagnetic indices that have the greatest influence on the wave distribution at a particular location and to determine the time delay between cause and effect. Then, we present models for wave magnetic field amplitude in the form of polynomial functions on control parameters that characterise geomagnetic activity for different equatorial regions of the magnetosphere. Finally, we analyse the precision of analytical models and define constraints on parameter values at which the models describe amplitudes of VLF/ELF waves adequately.

Table 1: List of control parameters from ERR analysis and its abbreviations used to develop wave activity models of the inner magnetosphere.

	Abbreviation	Description
1.	V_{sw}	hourly velocity of solar wind [km/s].
2.	N	hourly concentration of solar wind [cm^{-3}].
3.	P	Flow pressure of solar wind [nPa].
4.	AE	hourly AE index [nT].
5.	Dst	hourly Dst index [nT].
6.	Bt	IMF factor [nT].

2 Data description

The solar wind data and geomagnetic activity indices used for this study were obtained from OMNI website (<http://cdaweb.gsfc.nasa.gov>). Table 1 summarises the list of solar wind parameters and geomagnetic activity indices used as control parameters for the wave activity models in the inner magnetosphere. Bt is an IMF factor defined as $B_{tan} \sin^6(\theta/2)$ proposed by Balikhin *et al.* (2010); Boynton *et al.* (2011) (where $B_{tan} = \sqrt{B_x^2 + B_y^2}$ is the tangential IMF and $\theta = \tan^{-1}(B_y/B_z)$ is the clock angle of the IMF).

The wave data used in this study is registered by the search coil magnetometer instruments onboard the Cluster (Escoubet *et al.*, 2001) and THEMIS (Burch and Angelopoulos, 2009) spacecraft during the periods February 2001 to December 2010 and January 2007 to December 2014 respectively. Each of the three emission types is observed in their distinct frequency range. These frequency ranges were used to separate the different waves into three datasets, one for each emission. The three datasets contained the LBC, hiss and EMW wave magnitude in time, L-shell, Magnetic Local Time (MLT) and magnetic latitude.

The next step was to determine the spatial resolutions for each of the bins or sectors. This study only considered measurements in the vicinity of the equator for each of the

emission types. Therefore the spatial dimensions in magnetic latitude were between -20° and 20° . The bin size for the other two spatial dimensions was determined by data availability. Initially, the number of data points in each spatial bin covering 1 hour MLT and $1 R_E$ radially (with a range of 3-7 R_E) was determined. Data measurements in the range $3 < L < 4$ was not enough to study statistical properties of the wave activity in that region. Therefore, spatial bins were then combined at first radially into two bins covering $4 < L \leq 5$ and $5 < L < 7$ and then by MLT such that each of the spatial bins would contain over 1000 data points. These criteria arise because the ERR analysis requires around 1000 data points, covering a broad range of conditions, for reliable results.

Global distributions of the occurrence rate and root-mean-square (RMS) values of magnetic field amplitudes of whistler waves in chorus frequency range derived from THA observations during 2008-2014 are shown for different levels of magnetic activity in Figure 1. The corresponding orbital coverages are given in the smaller panels. From left to right, the models are presented for quiet ($K_p \leq 3$), moderate ($3 < K_p \leq 5$) and active ($K_p > 5$) conditions. The top row shows the distributions in L -shell / magnetic local time (MLT) domain with the dawn to the right and dusk to the left, while the bottom row shows the distributions in L -shell / magnetic latitude λ domain. The data is binned in steps of 1 L -shell, 1 h of MLT, 1° of λ . For a wide range of geomagnetic activity $0 < K_p < 7$ a vast amount of data is available for analysis, comprehensively covering all MLT and L -shells in the range 2-8. At higher geomagnetic activity levels the data coverage reduces considerably.

The occurrence rate is calculated as the ratio of a number of whistler waves with magnetic component greater than 4 pT to the total number of measurements in each bin. Whistler waves are observed over a broad MLT range from the midnight through dawn to the dusk sector (01:00-20:00 MLT). Note that the occurrence rate of whistler waves on the dayside is significantly higher than that of on the nightside that is consistent with Li *et al.* (2011). However, two regions with a high occurrence rate of whistler

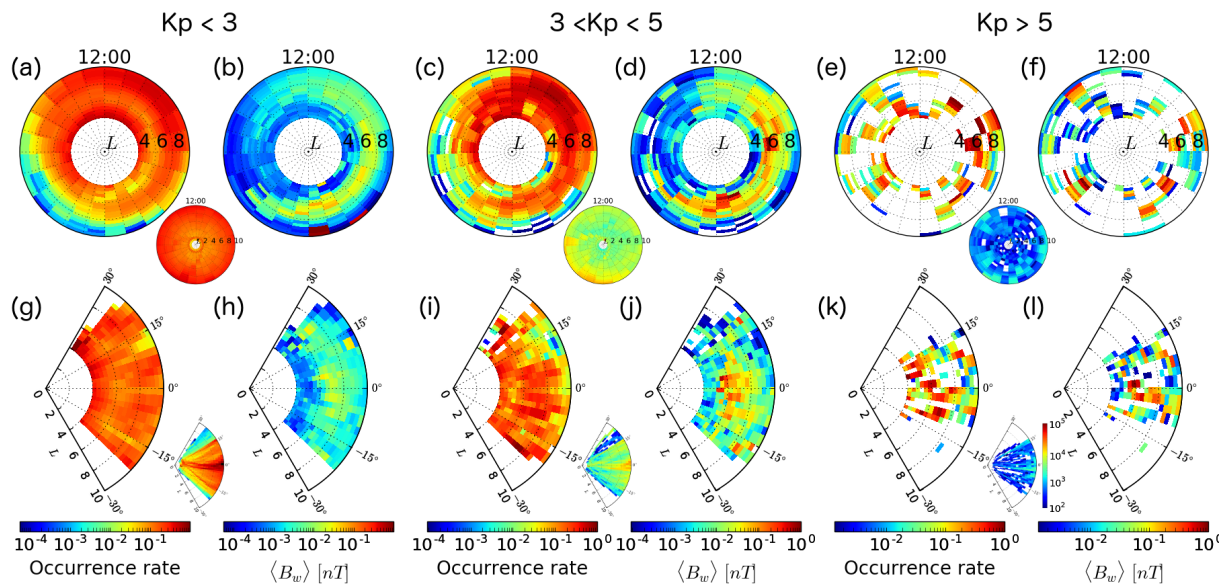


Figure 1: Occurrence rate of chorus emissions in L -shell/MLT domain for periods of low $K_p \leq 3$ (a), intermediate $3 < K_p \leq 5$ (c), and high geomagnetic activity $K_p > 5$ (e). RMS values of the magnetic component of chorus waves in L -shell/MLT domain for same levels of geomagnetic activity (b), (d), (f). Distributions for L -shell/ λ domain are shown on panels (g)-(l) in the same format. Corresponding orbital coverages of THA probe, colour coded, are shown in the small panels. The distributions are obtained using measurements of THA probe during 2008-2014.

waves can be distinguished. One at L -shells $4 < L < 6$, where whistler waves are mainly observed at 05:00-20:00 MLT and another at L -shells $6 < L < 8$, where whistler waves are observed at 00:00-15:00 MLT. The average amplitude distribution of electric and magnetic components of whistler waves are shown in Figure 1a, 1c, and 1e in L -shell/MLT domain. The typical magnetic component amplitude of whistler waves is greater than 10 pT over the entire region that extends from pre-midnight to the pre-noon sector (22:00-11:00 MLT) with the maximum at $6 < L < 8$. In the dusk sector (15:00-20:00 MLT) the magnetic component amplitude is lower than that observed in the morning sector by almost an order of magnitude. Even lower intensity waves are seen in the range 18:00-21:00 MLT at $4 < L < 6$. The occurrence rate and distributions of electric and magnetic components are in good agreement with those from previous studies by Meredith *et al.* (2003) based on CRRES measurements and by Pokhotelov *et al.* (2008) and Agapitov *et al.* (2011) based on early Cluster measurements (2001-2004).

3 Methodology

For this study, wave emission data registered by four Cluster and 3 THEMIS probes (THA, THD, and THE) was used. The dataset was formed on the basis of CDAWeb data. Wave amplitude of particular type was calculated using measurements from six channels of FBK instrument onboard THEMIS spacecraft or 27 channels of STAFF-SA instrument onboard Cluster spacecraft. Signals with an amplitude less than 1 pT were interpreted as noise and were extracted from the original dataset. Using local value of electron cyclotron frequency f_{ce} 3 frequency bands were determined for magnetosonic ($f < f_{LH}$), hiss ($f_{LH} < f < 0.1f_{ce}$) and lower band chorus ($0.1f_{ce} < f < 0.5f_{ce}$) waves. Wave amplitudes were calculated using signals from channels which central frequency lied within a particular frequency band. Resulting wave amplitude was defined as

$$A = \sqrt{\sum_{i=1}^n a_i A_i^2},$$

where n - number of channels (6 for FBK and 27 for STAFF-SA), A_i - signal amplitude of i -th channel and a_i indicates whether signal of i -th channel is used for resulting wave amplitude calculation. For example a_i for lower band chorus are defined as follows:

$$a_i = \begin{cases} 1, f_i \in [0.1f_{ce}; 0.5f_{ce}] \\ 0, f_i \notin [0.1f_{ce}; 0.5f_{ce}] \end{cases},$$

where f_i - central frequency for i -th channel. Resulting wave amplitudes and location of the probes described in MLT and L-shell are taken as the input data. These measurements were divided into different groups that belong to location bins for each wave type mentioned in Section 2. For each group distribution of RMS amplitude of magnetic wave field was built as a function of the two parameters with the greatest control over the wave activity. The Levenberg-Marquardt algorithm of nonlinear least squares fitting was then run for every distribution to calculate coefficients of the analytical representation of the model. The distributions of wave amplitudes were reproduced using third order polynomial function of control parameters:

$$\log_{10}(B_w) = \sum_{i=0}^3 \sum_{j=0}^3 a_{ij} cp_1^i cp_2^j \quad (1)$$

where B_w - RMS wave amplitude of the emission, cp_1 and cp_2 - a pair of control parameters that has the greatest influence on wave activity in particular spatial bin, and a_{ij} - coefficients of the model.

4 Analysis results

Results of the fitting for the three emission types at the different spatial bins can be found in the appendix (Tables 2-32). Figures 2-44 were constructed to illustrate the dependence of wave magnetic amplitudes of the three wave types on control parameters in different spatial bins and to compare with the results of the fitting. For each sector, there are two top control parameters of the emission type and corresponding time lags between the observed wave amplitude and the control parameters according to results of

ERR. The lags of the control parameters are indicated in brackets of the corresponding axis of the plot and expressed in hours. Panel (a) on Figures 2-44 shows number of measurements available at different levels of geomagnetic activity. Panel (b) illustrate a distribution of wave magnetic field amplitude in the domain of main control parameters for the given sector. Panel (c) shows the results of the analytical model for wave magnetic field amplitude obtained by fitting the polynomial function to the distribution on a panel (b). Panel (d) gives information about the discrepancies between the analytical model and the actual distribution. The axes of the panels(a-c) are labelled by the control parameters defined by ERR analysis with the most significant time lags in hours between the control parameter value and amplitude of the emission.

4.1 LBC wave models

The results show that either the AE index, Dst index or solar wind velocity have the largest ERR in all the sectors. The AE index has the largest control over the LBC at region 04:00-12:00 MLT and $4 < L < 7$ with time delays of 1 hour while for afternoon and dusk sectors from 12:00 to 22:00 main control parameter is Dst.

Figure 2 illustrates the model of magnetic wave amplitude of LBC for the spatial bin that extends $5 < L < 7$ and 04:00-08:00 MLT. Panel (a) shows the availability of LBC measurements in V_{sw} -AE domain with time lags of 1 and 10 hours for AE and V_{sw} indices. The colour represents the number of LBC waves registered by spacecraft in the current spatial bin at given geomagnetic conditions. It can clearly be seen that there is a vast amount of data available for wide range of geomagnetic activity $AE < 700$ nT and $300 < V_{sw} < 700$ km/s. However, as geomagnetic activity increases, the data coverage reduces considerably due to the rarity of such periods. The good coverage of the low latitude region of the inner magnetosphere provides the opportunity to study ELF/VLF emission properties during different magnetosphere activity conditions. It is clearly seen that quiet geomagnetic conditions ($AE < 100$ nT) are observed more often than disturbed. The RMS of magnetic wave amplitude on a panel (b) shows that for

quiet conditions average LBC amplitude is about 4-5 pT while for disturbed conditions the amplitude raises up to 20 pT. The values of RMS magnetic wave amplitude restored from the analytical model have similar values for quiet and disturbed conditions. Panel (d) shows a distribution of the discrepancies between the model and the observed values. 90% of model values differ from observed values less than 10%.

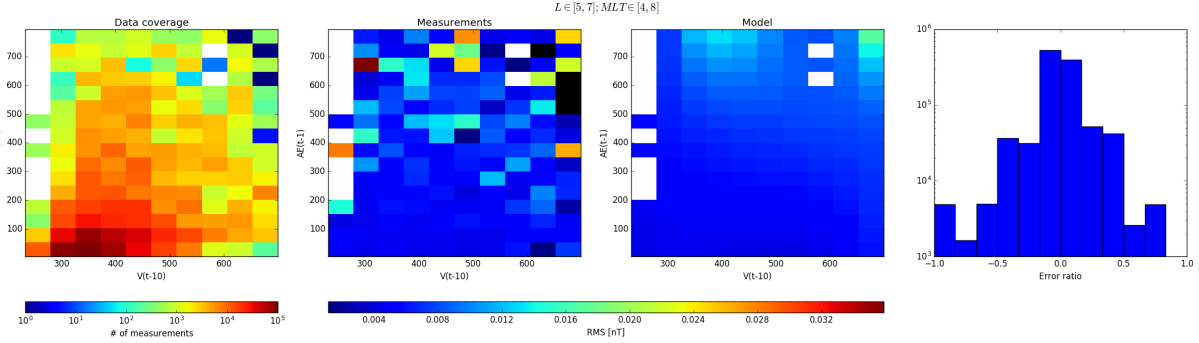


Figure 2: (a) Data coverage of the Cluster STAFF-SA and THEMIS FBK measurements in the LBC frequency range ($0.1\omega_{ce} < \omega < 0.5\omega_{ce}$) as a number of spectra captured in V_{sw} -AE domain for $5 < L < 7$ and 04 : 00 – 08 : 00 MLT. (b) RMS of LBC magnetic field amplitude in V_{sw} -AE domain measured by Cluster and THEMIS probes. (c) RMS values obtained from the analytical model developed using the measurements. (d) Distribution of discrepancies between analytical model and actual measurements.

Figure 3 illustrates the model of magnetic wave amplitude of LBC for the spatial bin that extends $4 < L \leq 5$ and 12:00-16:00 MLT. Panel (a) shows the availability of LBC measurements in an AE-Dst domain with time lags of 2 hours. The RMS of magnetic wave amplitude on a panel (b) shows that average LBC amplitude for quiet geomagnetic conditions ($Dst > -40$ nT) is about 3 pT, while during disturbed geomagnetic conditions RMS wave amplitude rises to 8 pT. Distribution of the discrepancies on a panel (d) shows 91% of model values differ from observed values less than 10%. However, due to small amount of measurements at $AE > 500$ nT magnetic wave amplitudes are diverse, and the model has significant deviations from the observed values.

Figure 4 illustrates the model of magnetic wave amplitude of LBC for the spatial bin that extends $5 < L < 7$ and 16:00-22:00 MLT. Panel (a) shows the availability of LBC measurements in V_{sw} -Dst domain with time lags of 1 and 4 hours for V_{sw} and Dst

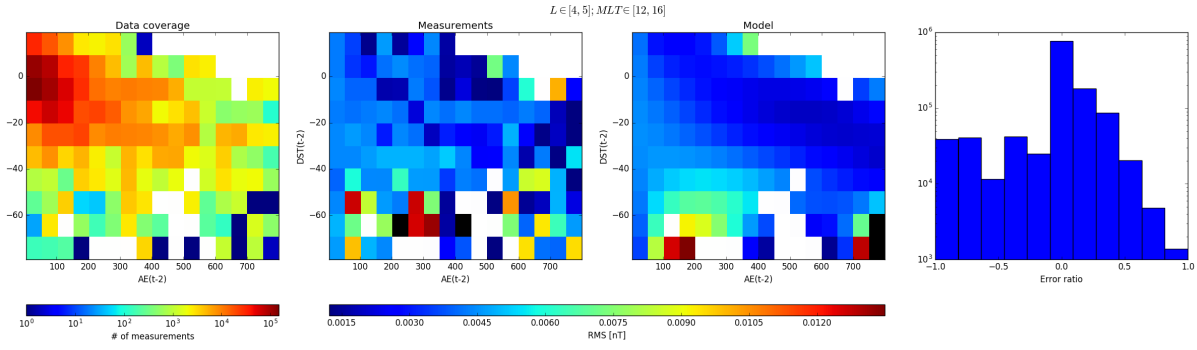


Figure 3: Data coverage, measured and analytical values of RMS of magnetic field amplitudes in AE-Dst domain for region $4 < L \leq 5$ and 12:00-16:00 MLT in same format as Figure 2.

indices. The RMS of magnetic wave amplitude on a panel (b) shows that average LBC amplitude is about 4.5-5.5 pT. Distribution of the discrepancies on a panel (d) shows 94% of model values differ from observed values less than 10%. However, due to small amount of measurements at $Dst < -40$ nT magnetic wave amplitudes are diverse and the model exhibit significant deviations from the observed values. Therefore the model describes adequately observed wave amplitudes for $Dst > -40$ nT.

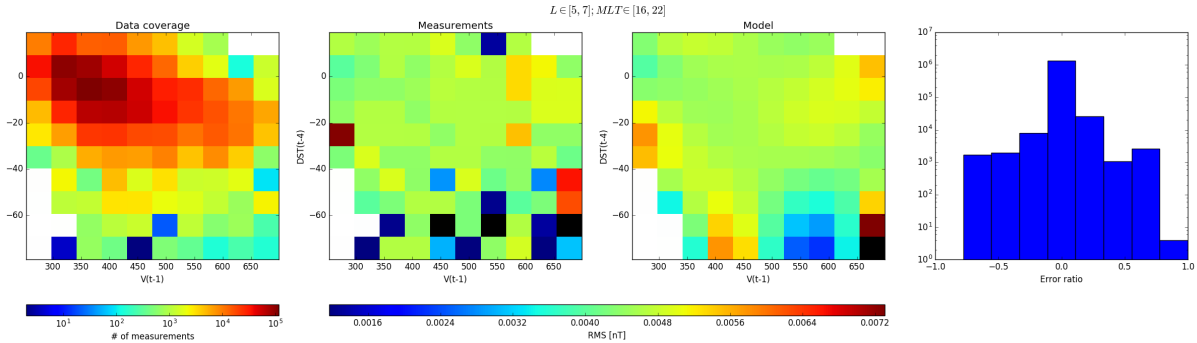


Figure 4: Data coverage, measured and analytical values of RMS of magnetic field amplitudes in V_{sw} -Dst domain for region $5 < L < 7$ and 16:00-22:00 MLT in same format as Figure 2.

Other figures that illustrate distributions of LBC wave amplitudes registered by spacecraft and calculated by developed models, as well as tables that contain values of the coefficients for models, are listed in Appendix A.

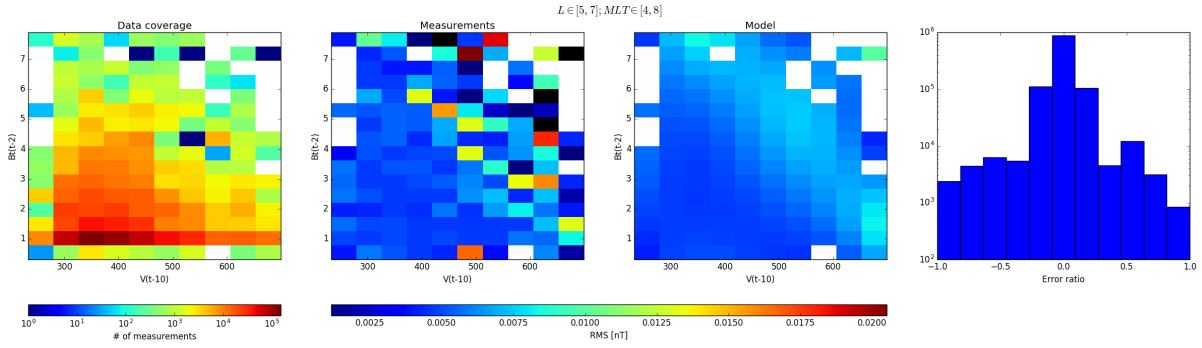


Figure 5: Data coverage, measured and analytical values of RMS of magnetic field amplitudes in V_{sw} - Bt domain for region $5 < L < 7$ and 04:00-08:00 MLT in same format as Figure 2.

4.2 Hiss wave models

The IMF factor has the largest influence on wave amplitudes from 22:00-08:00 MLT, with time lags between 1 and 3 hours. Figure 5 illustrates magnetic wave amplitudes of hiss for the spatial bin that extends $5 < L < 7$ and 04:00-08:00 MLT. Panel (a) shows the availability of hiss measurements in V_{sw} - Bt domain with time lags of 10 and 2 hours for V_{sw} and Bt indices. The RMS of magnetic wave amplitude on panel (b) shows that for quiet conditions ($V_{sw} < 500 \text{ km/s}$ and $Bt < 5$) average hiss amplitude is about 4-5 pT, while for disturbed conditions the amplitude raises up to 8 pT. Distribution of the discrepancies on a panel (d) shows 85% of model values differ from observed values less than 10%. The largest deviations from model are observed at active geomagnetic conditions for $V > 650 \text{ km/s}$ and $Bt > 6 \text{ nT}$ due to small amount of measurements.

Figure 6 illustrates the model of magnetic wave amplitude of hiss for the spatial bin that extends $4 < L \leq 5$ and 08:00-12:00 MLT. Panel (a) shows the availability of hiss measurements in V_{sw} - AE domain with time lags of 2 and 1 hours for V_{sw} and AE indices respectively. The RMS of magnetic wave amplitude on a panel (b) shows that average hiss amplitude for quiet geomagnetic conditions ($AE < 300 \text{ nT}$) is about 4 pT, while during disturbed geomagnetic conditions RMS wave amplitude rises to 8 pT. Distribution of the discrepancies on a panel (d) shows 93% of model values differ from observed values

less than 10%. However, due to small amount of measurements at $AE > 400$ nT and $V_{sw} > 500$ km/s the obtained model is not reliable.

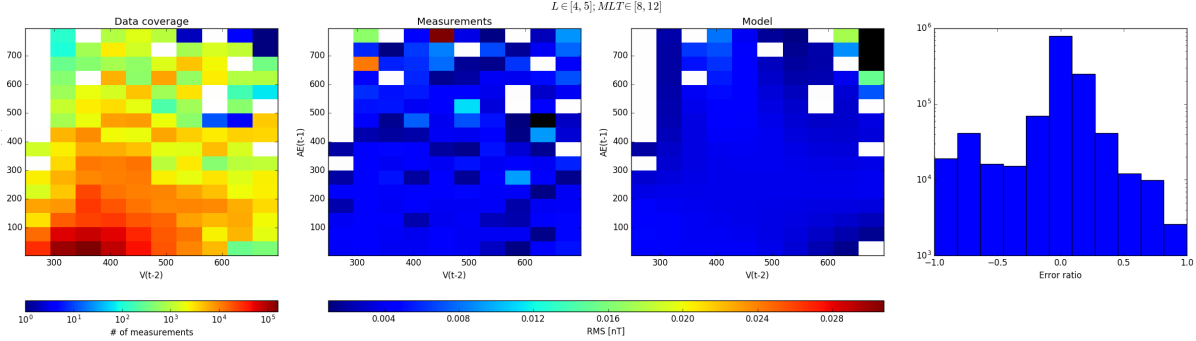


Figure 6: Data coverage, measured and analytical values of RMS of magnetic field amplitudes in V_{sw} -AE domain for region $4 < L \leq 5$ and 08:00-12:00 MLT in same format as Figure 2.

The Dst index has the highest ERR in the two pre-midnight sectors, both with a lag of 1 hour. Figure 7 illustrates magnetic wave amplitudes of hiss for the spatial bin that extends $5 < L < 7$ and 20:00-00:00 MLT. Panel (a) shows the availability of hiss measurements in a P-Dst domain with a time lag of 1 hour for P and Dst indices. The RMS of magnetic wave amplitude on a panel (b) shows that for quiet conditions ($Dst < -40$ nT and $P < 4$ nPa) average hiss amplitude is about 4-5 pT while for disturbed conditions the amplitude raises up to 8 pT. Distribution of the discrepancies on a panel (d) shows 85% of model values differ from observed values less than 10%. The largest deviations from the model are observed at active geomagnetic conditions for $P > 5$ due to a few measurements.

Other figures that illustrate distributions of hiss wave amplitudes registered by spacecraft and calculated by developed models, as well as tables that contain values of the coefficients for models, are listed in Appendix B.

4.3 EMW wave models

The Dst index has the most control of EMW waves in the inside sectors 16:00-04:00 MLT. Figure 8 illustrates magnetic wave amplitudes of EMW for the spatial bin that extends

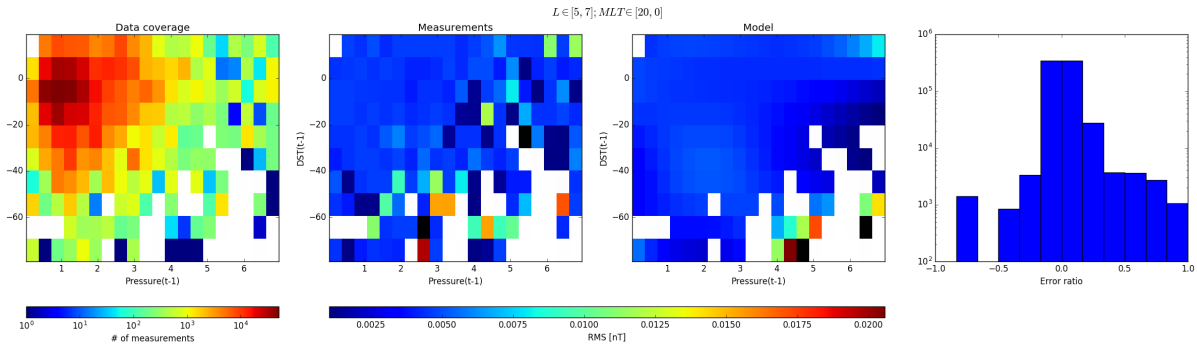


Figure 7: Data coverage, measured and analytical values of RMS of magnetic field amplitudes in P-Dst domain for region $5 < L < 7$ and 20:00-00:00 MLT in same format as Figure 2.

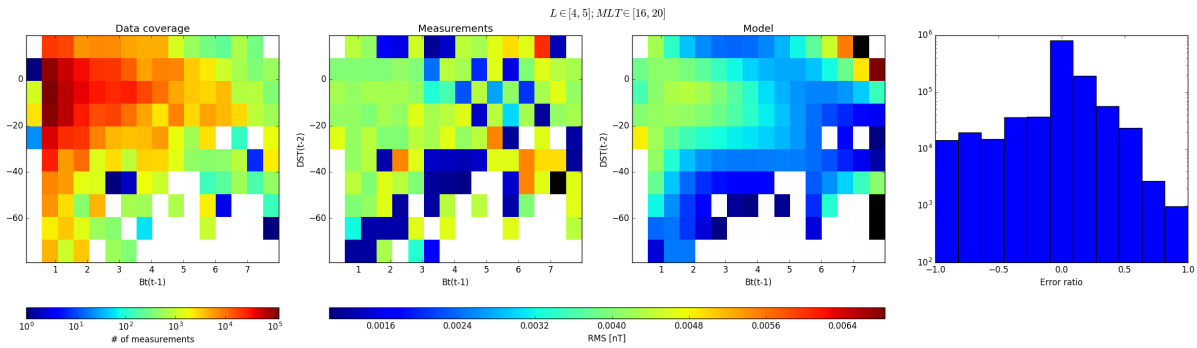


Figure 8: Data coverage, measured and analytical values of RMS of magnetic field amplitudes in Bt-Dst domain for region $4 < L \leq 5$ and 16:00-20:00 MLT in same format as Figure 2.

$4 < L \leq 5$ and 16:00-20:00 MLT. Panel (a) shows the availability of EMW measurements in a Bt-Dst domain with time lags of 1 and 2 hours for Bt and Dst indices. Average RMS of magnetic wave amplitude on a panel (b) is about 4.5 pT and doesn't have any pronounced dependence on control parameters. Distribution of the discrepancies on a panel (d) shows 92% of model values differ from observed values less than 10%. The model exhibits an artificial peak at $Bt > 7$ nT and $Dst < -60$ nT due to small amount of measurements.

The AE index controls the pre-noon and afternoon inside sectors and the noon and dusk outside sectors. Figure 9 illustrates magnetic wave amplitudes of EMW for the spatial bin that extends $5 < L < 7$ and 15:00-19:00 MLT. Panel (a) shows the availability

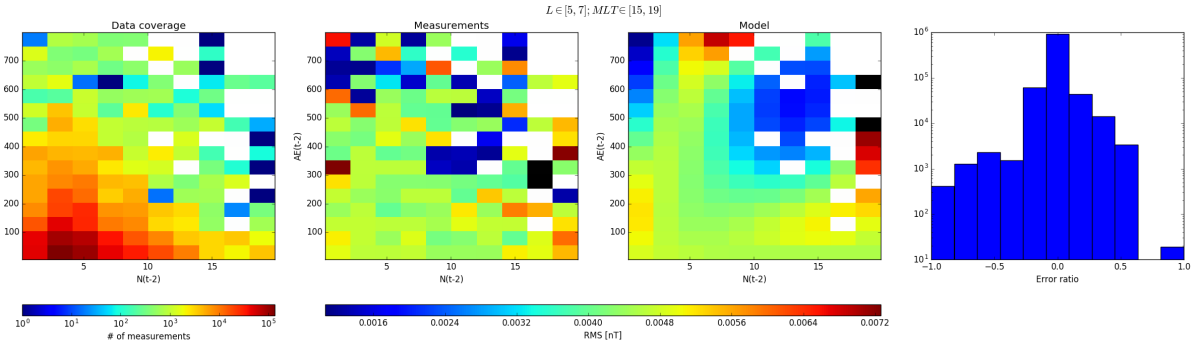


Figure 9: Data coverage, measured and analytical values of RMS of magnetic field amplitudes in N-AE domain for region $5 < L < 7$ and 15:00-19:00 MLT in same format as Figure 2.

of EMW measurements in N-AE domain with a time lag of 2 hours. The RMS of magnetic wave amplitude on panel (b) is about 4.5 pT and increases up to 6 pT at $N > 10 \text{ cm}^{-3}$. Distribution of the discrepancies on a panel (d) shows 97% of model values differ from observed values less than 10%.

Other figures that illustrate distributions of hiss wave amplitudes registered by spacecraft and calculated by developed models as well as tables that contain values of the coefficients for models are listed in Appendix C.

4.4 Models of simplified dependence on K_P

Many modern models of quasi-linear diffusion by whistler mode waves use parallel (or quasi-parallel) wave propagation $\theta \approx 0^\circ$ approximation (Albert, 2007; Glauert and Horne, 2005; Shprits *et al.*, 2006; Summers *et al.*, 2007). However, it has also been shown that whistler mode waves with very oblique $\theta \in [\theta_g, \theta_r]$ (where θ_g and θ_r are the Gendrin and resonance cone angles (Gendrin, 1961)) could play an important role for electron resonant pitch-angle scattering (Albert, 2012; Artemyev *et al.*, 2012; Glauert *et al.*, 2014; Li *et al.*, 2014; Ni *et al.*, 2013; Shprits and Ni, 2009).

Early studies of the chorus wave-normal angles distribution $g(\theta)$ by (Burton and Holzer, 1974; Goldstein and Tsurutani, 1984; Haque *et al.*, 2010; Hayakawa *et al.*, 1984; Lauben *et al.*, 2002) has shown that values of θ are generally less than 30° at $|\lambda| < 40^\circ$

and it rises up to 85° at $|\lambda| > 40^\circ$. However, recent observations of ELF/VLF emissions by THEMIS and Cluster missions have shown the existence of whistler mode waves with $\theta \in [60^\circ, 80^\circ]$ in equatorial region (Agapitov *et al.*, 2012; Li *et al.*, 2011). Despite the amplitude of quasi-perpendicular chorus waves is rather moderate, their ability for the resonant scattering of radiation belt electrons is significant (Albert, 2012; Artemyev *et al.*, 2012; Glauert *et al.*, 2014; Li *et al.*, 2014; Ni *et al.*, 2013; Shprits and Ni, 2009).

The $g(\theta)$ distribution derived from Cluster spacecraft observations has been approximated as a function of latitude for three geomagnetic activity ranges in the works by Artemyev *et al.* (2013a) and Mourenas *et al.* (2014). The distribution $g(\theta)$ was shown to depend on local coordinates (L -shell, MLT, and latitude) and geomagnetic activity. Agapitov *et al.* (2015) has proposed a statistical model of chorus amplitudes and obliquity parameter defined as the ratio of a number of quasi-perpendicular to quasi-parallel waves based on measurements registered during ten years of Cluster operation. Obtained models are defined as polynomial functions of L -shell, magnetic latitude, and geomagnetic activity.

However, previous studies used data registered by spacecraft with high inclinations of their orbits which lead to poor coverage of equatorial region at $5 < L < 7$ that is not sufficient for statistical study. In this section, we analyse RBSP data registered between 2012 and 2016 to develop empirical models of LBC and hiss wave parameters as a function of magnetic latitude λ and K_p index in the equatorial region $|\lambda| < 20^\circ$ at radial distances from 3 to 6 R_E . Also, we present models for wave-normal and wave magnetic field amplitude in the form of polynomial functions on L -shell, λ , and K_P for two MLT sectors.

Pitch-angle diffusion coefficients for electrons resonantly interacting with whistler mode waves can be written as (Glauert and Horne, 2005):

$$D_{\alpha\alpha} = \frac{e^2}{4\pi} \sum_n \int_{\theta_{min}}^{\theta_{max}} \frac{d\theta}{\cos\theta} \sum_i \frac{\hat{B}_w^2(\omega_i) \sin\theta \tilde{g}(\theta) |\Phi_{n,k}|^2}{N(\omega_i) |v_{\parallel} - \partial\omega/\partial k_{\parallel}|_{k_{\parallel i}}} \times \left(\frac{n\Omega_{ce}/\gamma - \omega_i \sin^2\alpha}{\cos\alpha} \right)^2 \quad (2)$$

where n is the harmonic number, i is the number of the resonant root, θ_{min} and θ_{max} are limits determined by the model used ($\theta_{min} = 0$ and θ_{max} is slightly below the resonance cone θ_{res} see details in Artemyev *et al.* (2013b)), and ω_i , k_i are solutions of equations:

$$\omega = \omega(k, \theta)$$

$$\omega - k_{\parallel} v_{\parallel} = -n\Omega_{ce}/\gamma$$

$\omega = \omega(k, \theta)$ is the dispersion relation, α is the particle pitch angle, $v_{\parallel} = \sqrt{1 - \gamma^{-2} \cos^2 \alpha}$, and γ is the relativistic factor. The function $\Phi_{n,k}$ describes the relation between the wave electric and magnetic field components (Glauert and Horne, 2005). All local system parameters (for given λ) are included into functions $G(\theta) = \sin(\theta)\tilde{g}(\theta)/N(\omega_i)$ and \hat{B}_w^2 . The latter defines the spectral distribution of wave intensity evaluated at the resonant root ω_i .

$$\hat{B}_w^2(\omega_i) = A \exp\left(-\frac{(\omega_m - \omega_i)^2}{\delta\omega^2}\right)$$

where A is the normalization constant, $\int_{\omega_{min}}^{\omega_{max}} \hat{B}_w^2(\omega) d\omega = B_w^2$, and $B_w^2(\lambda)$ is the local wave intensity. The function $G(\theta)$ gives the normalised distribution of wave magnetic energy as a function of θ at a given latitude

$$G(\theta) = 2\pi^2 \sin \theta \tilde{g}(\theta) \left(\int_{\theta_{min}}^{\theta_{max}} \sin \theta \tilde{g}(\theta) k^2 \frac{\partial k}{\partial \omega} \Big|_{\theta} d\theta \right)^{-1}$$

where $g(\theta)$ is the probability distribution function (PDF) at angle θ . This function determines the amount of wave energy with a wave-normal angle θ in the element of \mathbf{k}^3 space $dk^2 = \sin \theta k^2 dk d\theta$. Spacecraft measurements provide a number of waves in the elementary volume $k^2 dk d\theta$. Thus, measurements already provide the function $g(\theta) = \hat{g}(\theta) \sin \theta$. This function $g(\theta)$ can be approximated by two Gaussians (Artemyev *et al.*, 2013a; Mourenas *et al.*, 2014)

$$g(\theta) = \exp\left(-\frac{(\theta - \theta_1)^2}{\delta\theta_1^2}\right) + Q^2 \exp\left(-\frac{(\theta - \theta_2)^2}{\delta\theta_2^2}\right)$$

where the factor Q depends on K_P (or Dst), on L -shell, as well as on geomagnetic latitude and MLT. Parameters θ_1 , θ_2 , $\delta\theta_1 \approx \delta\theta_2$ are almost the same for dayside and nightside and do not depend strongly on L -shell either. Reasonable approximations for these parameters are $\theta_1 \approx 15^\circ$, $\theta_2 \approx 70^\circ$, and $\delta\theta_{1,2} \approx 10^\circ$.

Obliquity parameter Q is defined as ratio of the number of oblique waves to the total number of waves and is calculated using following expression:

$$Q = \sum_{i=0}^3 \sum_{j=0}^3 a_{ij} (\lambda[^\circ]/10)^i L^j \sum_{k=0}^3 b_k K_P^k, \quad (3)$$

where a_{ij} , b_k - coefficients, listed in tables 33-40, λ - magnetic latitude, L - L -shell, K_P - geomagnetic index.

RMS of wave amplitudes is calculated using following expression:

$$B_w = \sum_{i=0}^3 \sum_{j=0}^3 a_{ij} (\lambda[^\circ]/10)^i L^j \sum_{k=0}^3 b_k K_P^k, \quad (4)$$

where a_{ij} , b_k - coefficients, listed in tables 41-48, λ - magnetic latitude, L - L -shell, K_P - geomagnetic index.

Figure 10 illustrates the model of obliquity parameter distribution of LBC in λ - K_P domain for four L -shell ranges and two ranges in MLT. The colour codes the value of the obliquity parameter. Overall, obliquity parameter tends to increase with K_P from 0.01 at $K_P < 1+$ to 0.6 at higher values of K_P . However, the dependence of obliquity parameter on λ is more complicated. Inside the plasmasphere obliquity parameter has one maximum around $\lambda \approx 20^\circ$ and $2 < L < 3$ and $\lambda \approx 15^\circ$ at $3 < L < 4$. Outside the plasmasphere $5 < L < 7$ in the night sector 15:00 - 03:00 MLT obliquity parameter has two expressed maximums at 5° and 20° , whereas in the day sector 03:00 - 15:00 MLT the two maximums are significantly less pronounced.

Figure 11 illustrates the model of magnetic amplitude B_w distribution of LBC in λ - K_P domain for four L -shell ranges and two ranges in MLT. Overall, magnetic amplitude B_w is strongly dependent on L -shell, λ , and K_P . It is clearly seen that minimum and maximum

values of B_w rise with L -shell in both day and night sectors. The increase of B_w with geomagnetic activity is evident on all panels. Magnetic amplitude B_w has two maximums at $\lambda \approx 5^\circ$ and $\lambda \approx 20^\circ$ in L -shell range $4 < L < 7$ in both day and night sectors.

Although, the obliquity parameter for hiss waves tends to decrease with L -shell, as can be seen from figure 12, generally the value of the obliquity parameter is considerably lower than for LBC waves. Also, there is no significant dependence of obliquity parameter on λ and K_P . Most values of the obliquity parameter lie within range $4.0 \times 10^{-4} - 1 \times 10^{-2}$. Figure 13 shows the distributions of the magnetic wave amplitude B_w of hiss waves. In contrast to LBC waves, hiss wave amplitudes show a weak dependence on λ . However, for $5 < L < 7$ the maximum of hiss amplitudes is confined in the equatorial region $\lambda < 5^\circ$. Inside the plasmasphere a weak dependence of hiss magnetic amplitude on the K_P index is visible. The slight decline of B_w for high geomagnetic conditions $K_P > 7$ can not be reliable due to sparse measurements for $K_P > 6+$.

4.5 Hiss intensity latitudinal extent

Whistler waves of hiss type are known to be the natural phenomenon of the plasmasphere (Malaspina *et al.*, 2016). Plasmaspheric hiss amplitudes are dependent on L -shell, MLT and geomagnetic activity, with two distinct latitudinal zones of peak wave activity, primarily on the dayside (Agapitov *et al.*, 2011, 2013; Agapitov *et al.*, 2014; Green *et al.*, 2005; Malaspina *et al.*, 2016; Meredith *et al.*, 2004; Spasojevic *et al.*, 2015). The distribution of wave normal angles is mostly quasi-parallel in a vicinity of the geomagnetic equator with a strong dependence on λ with simplified dependence of the distribution maximum $\theta \approx 2.1\lambda$. Dependence of hiss amplitude on λ (up to 40°) is weak (Agapitov *et al.*, 2011, 2013; Spasojevic *et al.*, 2015) that shows absence of hiss source and significant wave amplification/damping in the plasmasphere; so, the equatorial values of amplitude can be a good estimation for hiss amplitude up to $\lambda \approx 30 - 35^\circ$. The best coverage of middle and high latitudes by VLF measurements was from Cluster (Agapitov *et al.*, 2011, 2013; Pokhotelov *et al.*, 2008), AKEBONO (Agapitov *et al.*, 2014), and DE1 (Green

et al., 2005) projects, and these measurements mostly confirmed a weak dependence on λ with the possible presence of high latitude (above 45°) additional separated wave source. Results presented in (Meredith *et al.*, 2004) with a secondary maximum at $\lambda \sim 25 - 30^\circ$ were based on CRRES data (electric field VLF measurements only) and could demonstrate variation with λ of wave normal angle distribution.

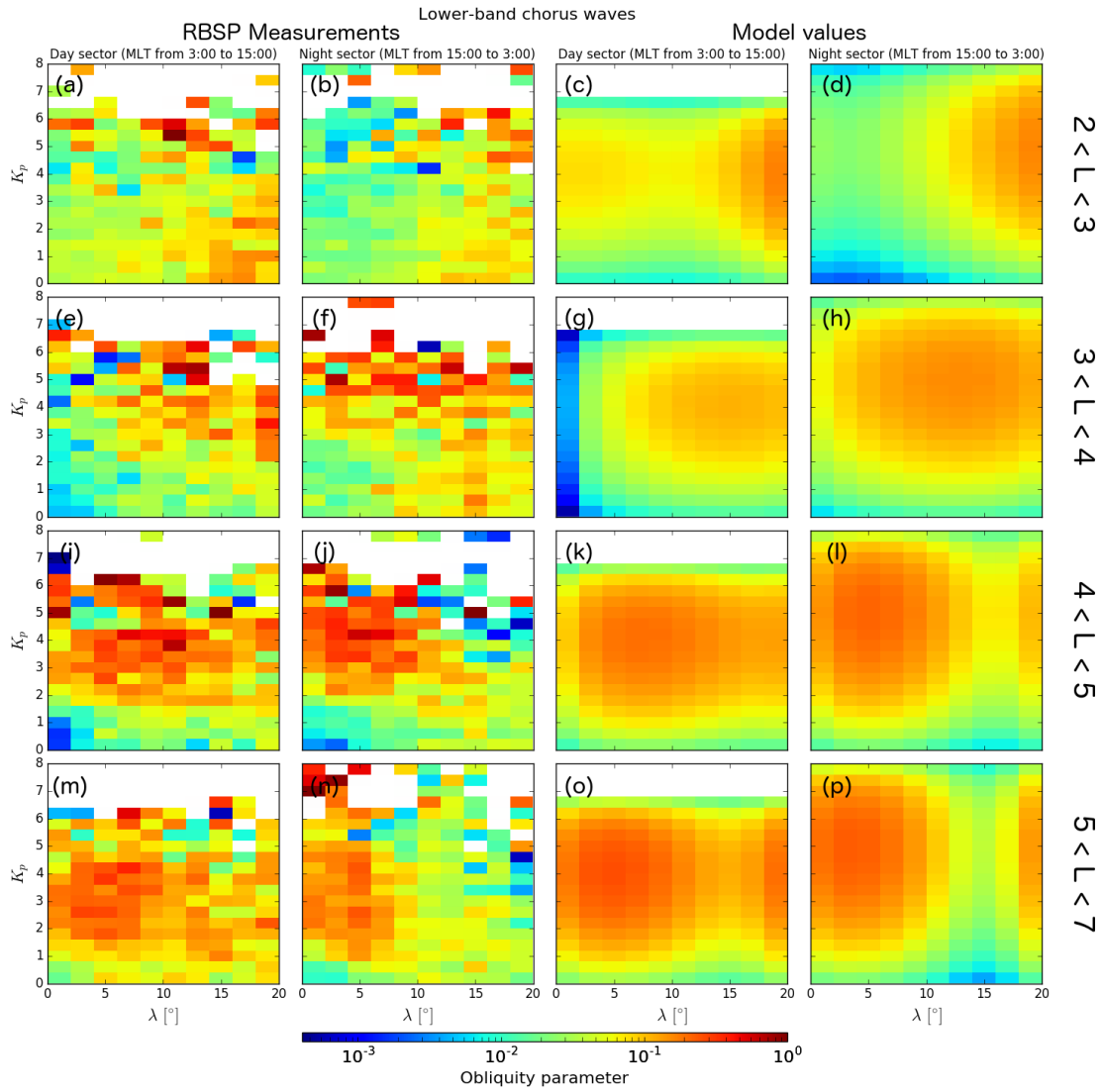


Figure 10: Distribution of the obliquity parameter of LBC waves in λ - K_P domain according to measurement registered by RBSP probes during 2012-2015, (two left columns), and according to simplified models given by (3) (two right columns).

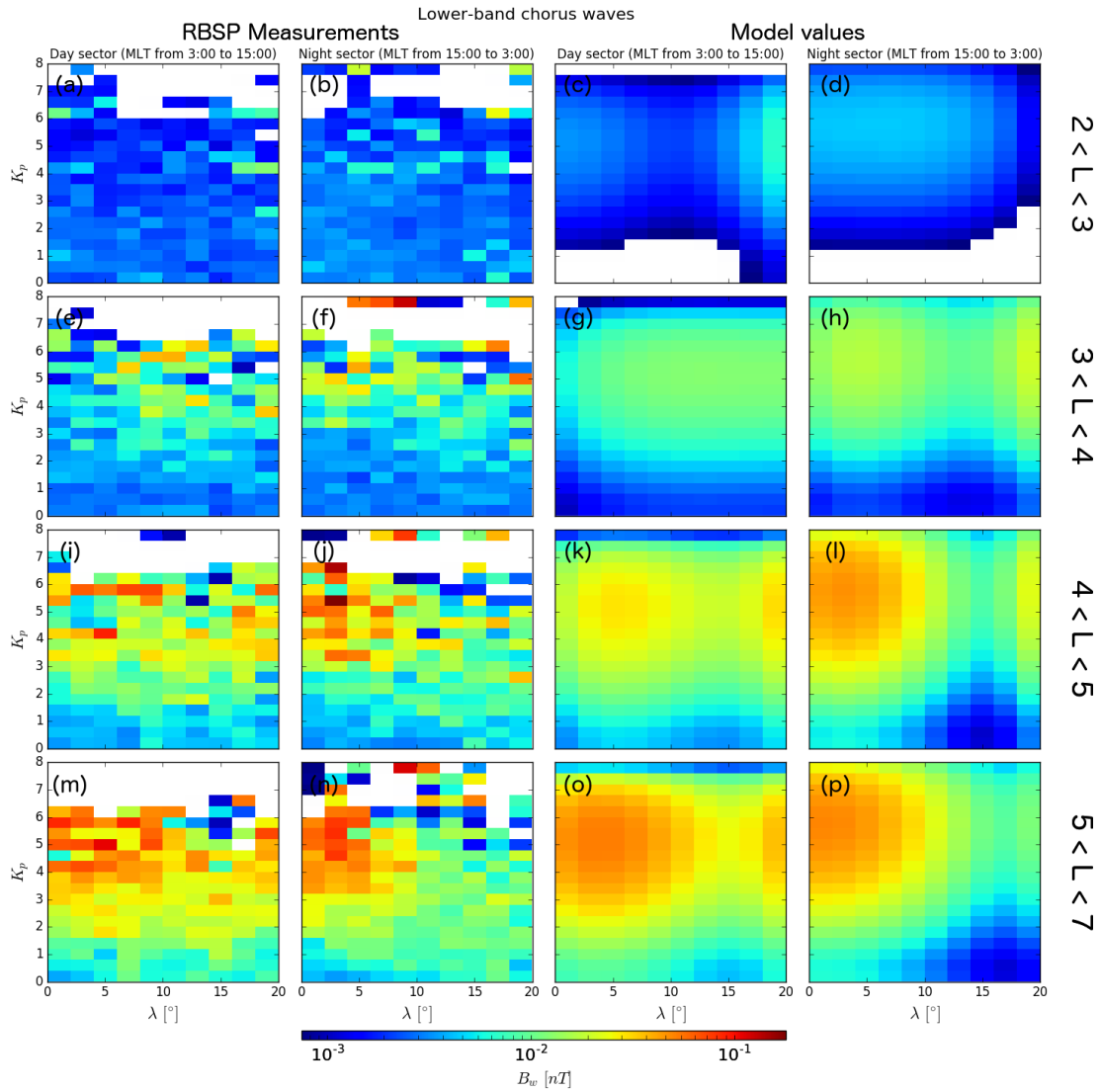


Figure 11: Distribution of the RMS amplitude of LBC waves in λ - K_P domain according to measurement registered by RBSP probes during 2012-2015, (two left columns), and according to simplified models given by (3) (two right columns).

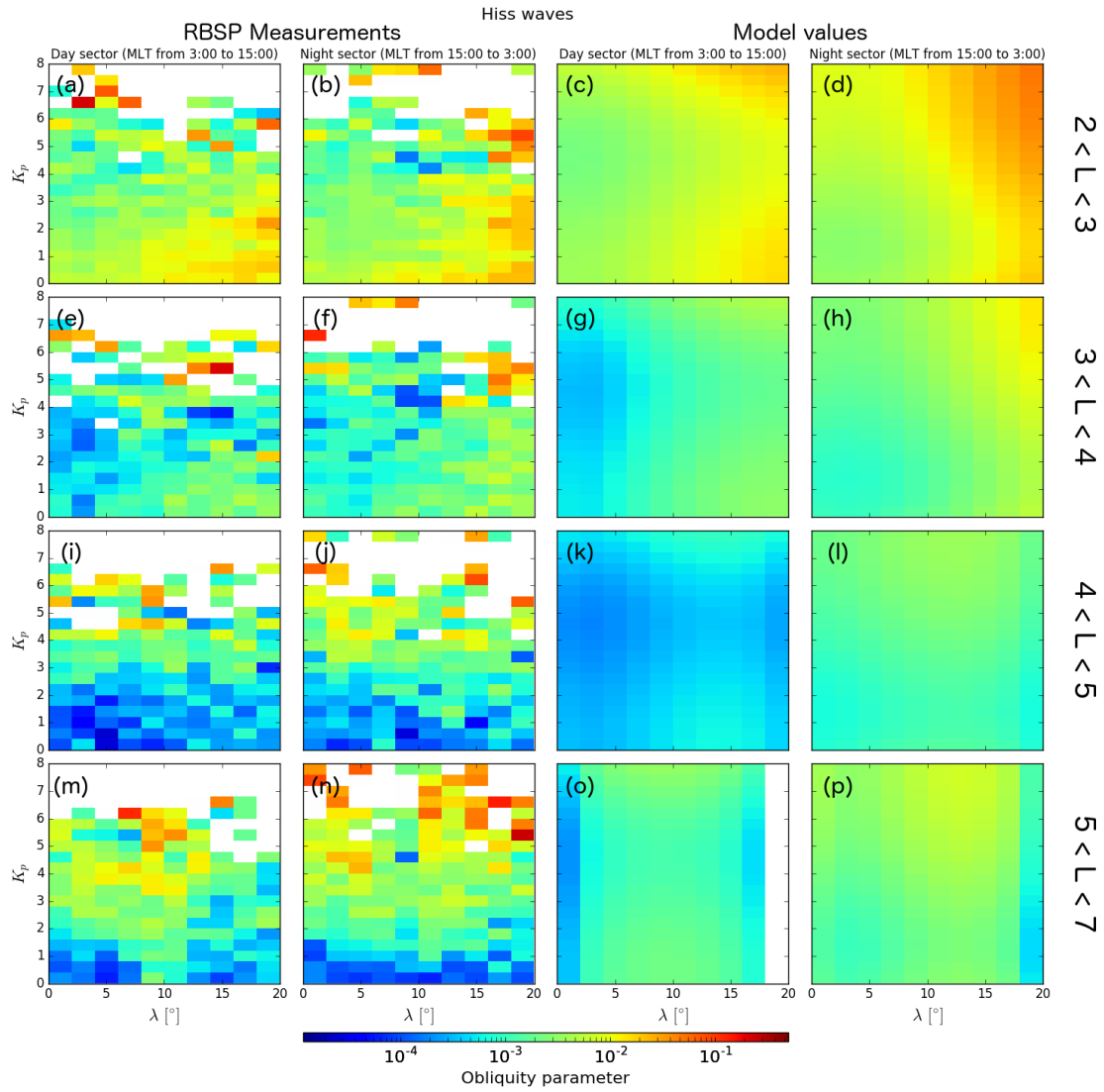


Figure 12: Distribution of the obliquity parameter of hiss waves in λ - K_P domain according to measurement registered by RBSP probes during 2012-2015, (two left columns), and according to simplified models given by (3) (two right columns).

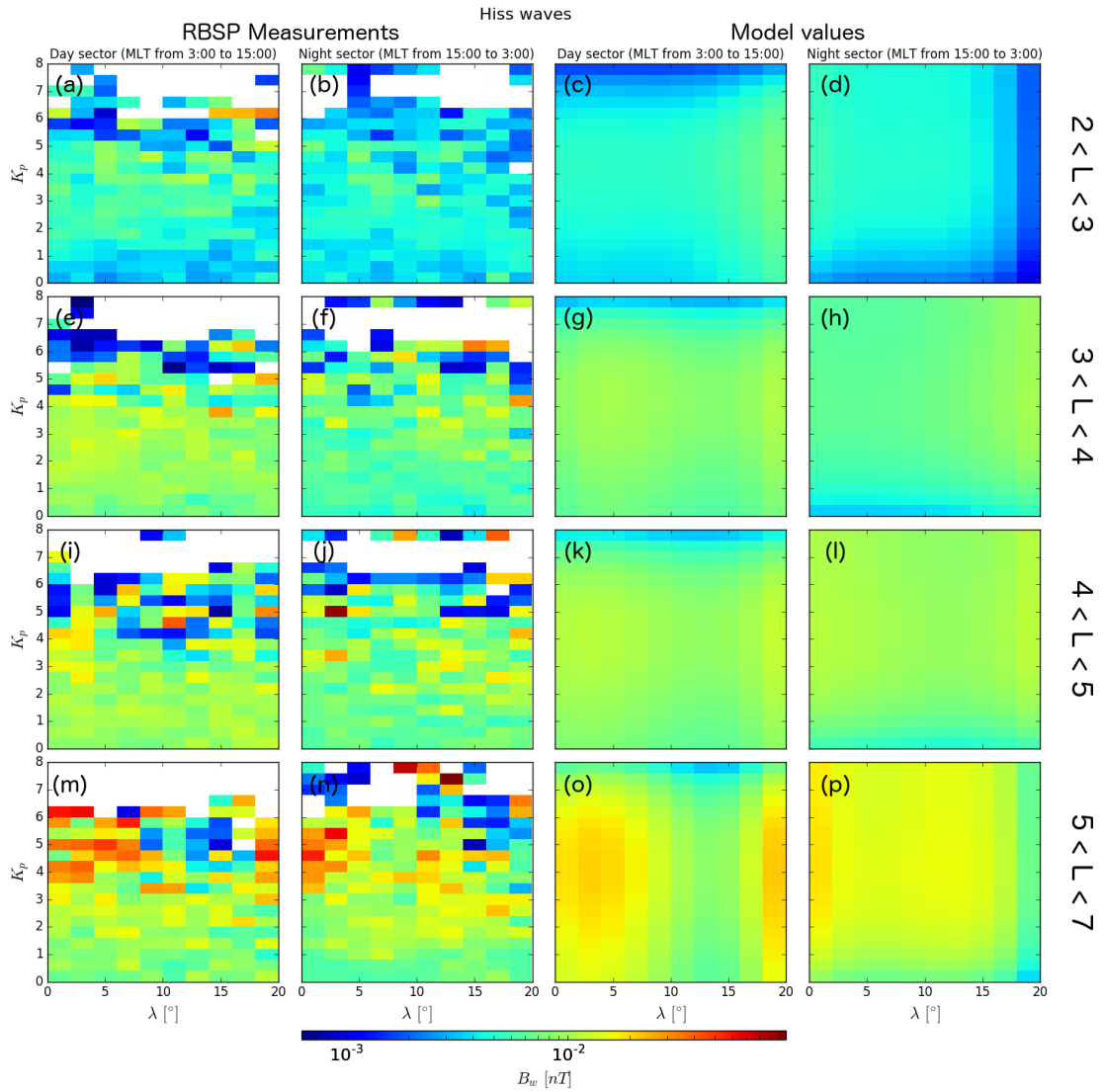


Figure 13: Distribution of the RMS amplitude of hiss waves in λ - K_P domain according to measurement registered by RBSP probes during 2012-2015, (two left columns), and according to simplified models given by (4) (two right columns).

5 Database description

The database contains models of RMS values of magnetic field amplitudes for three emission types in the inner magnetosphere $4 < L < 7$. The database consists of 31 ASCII-coded files, which have following naming convention:

$$\{wave_type\}-L-\{L_{min}\}-\{L_{max}\}-MLT-\{MLT_{min}\}-\{MLT_{max}\}.txt,$$

where *wave_type* - type of the VLF/ELF emission $\{ems, hiss, lbc\}$, L_{min} , L_{max} , MLT_{min} , MLT_{max} - designate boundaries of the spatial bin. Each file is composed of a header, specifying the spatial region, control parameters, and time lags used in the model, coefficients required to calculate RMS values of magnetic amplitudes using equation 1.

Appendix E provides code snippets that can serve as examples of how to load models from the files and calculate magnetic field amplitudes using some common languages.

6 Conclusions

We collected database of whistler waves observation in a vicinity of the geomagnetic equator (chorus generation region). It is found that vast amount of data is available to be analysed, comprehensively covering all magnetic local times (MLT) and L -shell in the range $4 < L < 7$ for a wide range of geomagnetic activity $K_p \in [0, 6]$.

The new statistical wave models are built concerning the lags of the geomagnetic indices and solar wind parameters identified by ERR and therefore account the previous evolution of the magnetosphere's state. New wave parameterizations obtained in present deliverable provide such an information of the distributions of wave amplitudes on a statistical basis, building on the very large and comprehensive database of LBC, hiss, and EMW measurements obtained over ten years by the Cluster spacecraft and seven years of THEMIS spacecraft. The polynomial wave models provide the needed information as a function of geomagnetic activity, as described by two most influential parameters. This could allow future detailed studies concerning the better relevance of one parameter

as compared to the other in various space weather simulations or related to their likely complementarity in some parameter ranges as regards the information provided on the wave distribution.

Numerical calculations of wave-particle scattering on the basis of the proposed wave models should hopefully allow an improved forecasting ability in the outer belt, while at the same time enabling the full numerical codes, for the first time, to study the different effects of control parameters' disturbances (roughly corresponding to substorms and storms) in shaping the Earth's outer radiation belt.

References

- Agapitov, O., Krasnoselskikh, V., Zaliznyak, Y., Angelopoulos, V., Le Contel, O., and Rolland, G. (2010). Chorus source region localization in the Earth's outer magnetosphere using THEMIS measurements. *Annales Geophysicae*, **28**, 1377–1386.
- Agapitov, O., Krasnoselskikh, V., Dudok de Wit, T., Khotyaintsev, Y., Pickett, J. S., Santolík, O., and Rolland, G. (2011). Multispacecraft observations of chorus emissions as a tool for the plasma density fluctuations' remote sensing. *Journal of Geophysical Research (Space Physics)*, **116**, 9222.
- Agapitov, O., Krasnoselskikh, V., Khotyaintsev, Y. V., and Rolland, G. (2011). A statistical study of the propagation characteristics of whistler waves observed by Cluster. *Geophys. Res. Lett.*, **38**(20), 20103.
- Agapitov, O., Krasnoselskikh, V., Zaliznyak, Y., Angelopoulos, V., Le Contel, O., and Rolland, G. (2011). Observations and modeling of forward and reflected chorus waves captured by themis. *Annales Geophysicae*, **29**, 541–550.
- Agapitov, O., Krasnoselskikh, V., Khotyaintsev, Y. V., and Rolland, G. (2012). Correction to “a statistical study of the propagation characteristics of whistler waves observed by Cluster”. *Geophys. Res. Lett.*, **39**(24), 24102.

- Agapitov, O., Artemyev, A., Krasnoselskikh, V., Khotyaintsev, Y. V., Mourenas, D., Breuillard, H., Balikhin, M., and Rolland, G. (2013). Statistics of whistler mode waves in the outer radiation belt: Cluster STAFF-SA measurements. *J. Geophys. Res.*, **118**(6), 3407–3420.
- Agapitov, O. V., Artemyev, A. V., Mourenas, D., Kasahara, Y., and Krasnoselskikh, V. (2014). Inner belt and slot region electron lifetimes and energization rates based on akebono statistics of whistler waves. *J. Geophys. Res.*, **119**, 2876–2893.
- Agapitov, O. V., Artemyev, A. V., Mourenas, D., Mozer, F. S., and Krasnoselskikh, V. (2015). Empirical model of lower band chorus wave distribution in the outer radiation belt. *Journal of Geophysical Research (Space Physics)*, **120**, 10.
- Albert, J. M. (2007). Simple approximations of quasi-linear diffusion coefficients. *Journal of Geophysical Research (Space Physics)*, **112**, A12 202.
- Albert, J. M. (2008). Efficient approximations of quasi-linear diffusion coefficients in the radiation belts. *Journal of Geophysical Research (Space Physics)*, **113**, A06 208.
- Albert, J. M. (2012). Dependence of quasi-linear diffusion coefficients on wave parameters. *Journal of Geophysical Research (Space Physics)*, **117**, A09 224.
- André, R., Lefeuvre, F., Simonet, F., and Inan, U. S. (2002). A first approach to model the low-frequency wave activity in the plasmasphere. *Annales Geophysicae*, **20**, 981–996.
- Artemyev, A., Agapitov, O., Breuillard, H., Krasnoselskikh, V., and Rolland, G. (2012). Electron pitch-angle diffusion in radiation belts: The effects of whistler wave oblique propagation. *Geophys. Res. Lett.*, **39**, 8105.
- Artemyev, A., Agapitov, O., Krasnoselskikh, V., Breuillard, H., and Rolland, G. (2012). Statistical model of electron pitch angle diffusion in the outer radiation belt. *Journal of Geophysical Research (Space Physics)*, **117**, A08 219.

-
- Artemyev, A. V., Agapitov, O. V., Mourenas, D., Krasnoselskikh, V., and Zelenyi, L. M. (2013a). Storm-induced energization of radiation belt electrons: Effect of wave obliquity. *Geophys. Res. Lett.*, **40**, 4138–4143.
- Artemyev, A. V., Mourenas, D., Agapitov, O. V., and Krasnoselskikh, V. V. (2013b). Parametric validations of analytical lifetime estimates for radiation belt electron diffusion by whistler waves. *Ann. Geophys.*, **31**, 599–624.
- Balikhin, M. A., Boynton, R. J., Billings, S. A., Gedalin, M., Ganushkina, N., Coca, D., and Wei, H. (2010). Data based quest for solar wind-magnetosphere coupling function. *Geophys. Res. Lett.*, **37**, L24 107.
- Balikhin, M. A., Boynton, R. J., Walker, S. N., Borovsky, J. E., Billings, S. A., and Wei, H. L. (2011). Using the narmax approach to model the evolution of energetic electrons fluxes at geostationary orbit. *Geophys. Res. Lett.*, **38**, L18 105.
- Blum, L. W., Agapitov, O., Bonnell, J. W., Kletzing, C., and Wygant, J. (2016). Emic wave spatial and coherence scales as determined from multipoint van allen probe measurements. *Geophys. Res. Lett.*, **43**, 4799–4807.
- Boynton, R. J., Balikhin, M. A., Billings, S. A., Wei, H. L., and Ganushkina, N. (2011). Using the NARMAX OLS-ERR algorithm to obtain the most influential coupling functions that affect the evolution of the magnetosphere. *Journal of Geophysical Research (Space Physics)*, **116**, A05 218.
- Boynton, R. J., Balikhin, M. A., Billings, S. A., Reeves, G. D., Ganushkina, N., Gedalin, M., Amariutei, O. A., Borovsky, J. E., and Walker, S. N. (2013). The analysis of electron fluxes at geosynchronous orbit employing a narmax approach. *Journal of Geophysical Research (Space Physics)*, **118**, 1500–1513.
- Burch, J. L. and Angelopoulos, V. (2009). *The THEMIS Mission*. Springer New York, ISBN 978-0-387-89819-3.

- Burton, R. K. and Holzer, R. E. (1974). The origin and propagation of chorus in the outer magnetosphere. *J. Geophys. Res.*, **79**(7), 1014–1023.
- Cully, C., Bonnell, J., and Ergun, R. (2008). THEMIS observations of long-lived regions of large-amplitude whistler waves in the inner magnetosphere. *Geophys. Res. Lett.*, **35**(17).
- Escoubet, C. P., Fehringer, M., and Goldstein, M. (2001). Introduction to the cluster mission. *Annales Geophysicae*, **19**(10/12), 1197–1200. URL <http://www.ann-geophys.net/19/1197/2001/>.
- Gendrin, R. (1961). Le guidage des whistlers par le champ magnetique. *Planetary and Space Science*, **5**, 274.
- Glauert, S. A. and Horne, R. B. (2005). Calculation of pitch angle and energy diffusion coefficients with the padie code. *Journal of Geophysical Research (Space Physics)*, **110**, A04206.
- Glauert, S. A., Horne, R. B., and Meredith, N. P. (2014). Three-dimensional electron radiation belt simulations using the BAS Radiation Belt Model with new diffusion models for chorus, plasmaspheric hiss, and lightning-generated whistlers. *Journal of Geophysical Research (Space Physics)*, **119**, 268–289.
- Goldstein, B. E. and Tsurutani, B. T. (1984). Wave normal directions of chorus near the equatorial source region. *J. Geophys. Res.*, **89**(A5), 2789–2810.
- Green, J. L., Boardsen, S., Garcia, L., Taylor, W., Fung, S. F., and Reinisch, B. (2005). On the origin of whistler mode radiation in the plasmasphere. *J. Geophys. Res.*, **110**(A3), 3201.
- Gurnett, D. and Inan, U. (1988). Plasma wave observations with the dynamics explorer 1 spacecraft. *Rev. Geophys.*, **26**(2), 285–316.

- Haque, N., Spasojevic, M., Santolík, O., and Inan, U. S. (2010). Wave normal angles of magnetospheric chorus emissions observed on the Polar spacecraft. *Journal of Geophysical Research (Space Physics)*, **115**, A00F07.
- Hayakawa, M., Yamanaka, Y., Parrot, M., and Lefeuvre, F. (1984). The wave normals of magnetospheric chorus emissions observed on board GEOS 2. *J. Geophys. Res.*, **89**, 2811–2821.
- Helliwell, R. A. (1965). *Whistlers and Related Ionospheric Phenomena*.
- Horne, R. B., Thorne, R. M., Glauert, S. A., Albert, J. M., Meredith, N. P., and Anderson, R. R. (2005a). Timescale for radiation belt electron acceleration by whistler mode chorus waves. *J. Geophys. Res.*, **110**(A3).
- Horne, R. B., Thorne, R. M., Shprits, Y. Y., Meredith, N. P., Glauert, S. A., Smith, A. J., Kanekal, S. G., Baker, D. N., Engebretson, M. J., Posch, J. L., *et al.* (2005b). Wave acceleration of electrons in the van allen radiation belts. *Nature*, **437**(7056), 227–230.
- Horne, R. B., Glauert, S. A., Meredith, N. P., Boscher, D., Maget, V., Heynderickx, D., and Pitchford, D. (2013). Space weather impacts on satellites and forecasting the earth’s electron radiation belts with spacecast. *Space Weather*, **11**, 169–186.
- Kellerman, A. C., Shprits, Y. Y., and Turner, D. L. (2013). A geosynchronous radiation belt electron empirical prediction (greet) model. *Space Weather*, **11**, 463–475.
- Kennel, C. F. and Petschek, H. E. (1966). Limit on stably trapped particle fluxes. *J. Geophys. Res.*, **71**, 1.
- Koons, H. C. and Roeder, J. L. (1990). A survey of equatorial magnetospheric wave activity between 5 and 8 R(E). *Planet. Space Sci.*, **38**, 1335–1341.
- Lauben, D. S., Inan, U. S., Bell, T. F., and Gurnett, D. A. (2002). Source characteristics of ELF/VLF chorus. *Journal of Geophysical Research (Space Physics)*, **107**, 1429.

-
- Li, W., Bortnik, J., Thorne, R. M., and Angelopoulos, V. (2011). Global distribution of wave amplitudes and wave normal angles of chorus waves using THEMIS wave observations. *Journal of Geophysical Research (Space Physics)*, **116**(A15), 12 205.
- Li, W., Thorne, R. M., Bortnik, J., Reeves, G. D., Kletzing, C. A., Kurth, W. S., Hospodarsky, G. B., Spence, H. E., Blake, J. B., Fennell, J. F., Claudepierre, S. G., Wygant, J. R., and Thaller, S. A. (2013). An unusual enhancement of low-frequency plasmaspheric hiss in the outer plasmasphere associated with substorm-injected electrons. *Geophys. Res. Lett.*, **40**, 3798–3803.
- Li, W., Mourenas, D., Artemyev, A. V., Agapitov, O. V., Bortnik, J., Albert, J. M., Thorne, R. M., Ni, B., Kletzing, C. A., Kurth, W. S., and Hospodarsky, G. B. (2014). Evidence of stronger pitch angle scattering loss caused by oblique whistler-mode waves as compared with quasi-parallel waves. *Geophys. Res. Lett.*, **41**, 6063–6070.
- Malaspina, D. M., Jaynes, A. N., Boul, C., Bortnik, J., Thaller, S. A., Ergun, R. E., Kletzing, C. A., and Wygant, J. R. (2016). The distribution of plasmaspheric hiss wave power with respect to plasmopause location. *Geophysical Research Letters*, **43**(15), 7878–7886. ISSN 1944-8007. URL <http://dx.doi.org/10.1002/2016GL069982>. 2016GL069982.
- Meredith, N. P., Horne, R. B., and Anderson, R. R. (2001). Substorm dependence of chorus amplitudes: Implications for the acceleration of electrons to relativistic energies. *J. Geophys. Res.*, **106**, 13 165–13 178.
- Meredith, N. P., Horne, R. B., Thorne, R. M., and Anderson, R. R. (2003). Favored regions for chorus-driven electron acceleration to relativistic energies in the earth’s outer radiation belt. *Geophys. Res. Lett.*, **30**(16), 1871.
- Meredith, N. P., Horne, R. B., Thorne, R. M., Summers, D., and Anderson, R. R. (2004). Substorm dependence of plasmaspheric hiss. *J. Geophys. Res.*, **109**(A6), 6209.

-
- Mourenas, D. and Ripoll, J.-F. (2012). Analytical estimates of quasi-linear diffusion coefficients and electron lifetimes in the inner radiation belt. *J. Geophys. Res.*, **117**, 1204.
- Mourenas, D., Artemyev, A. V., Ripoll, J.-F., Agapitov, O. V., and Krasnoselskikh, V. V. (2012). Timescales for electron quasi-linear diffusion by parallel and oblique lower-band chorus waves. *Journal of Geophysical Research (Space Physics)*, **117**, A06 234.
- Mourenas, D., Artemyev, A., Agapitov, O., and Krasnoselskikh, V. (2013). Analytical estimates of electron quasi-linear diffusion by fast magnetosonic waves. *Journal of Geophysical Research: Space Physics*, **118**(6), 3096–3112.
- Mourenas, D., Artemyev, A. V., Agapitov, O. V., and Krasnoselskikh, V. (2014). Consequences of geomagnetic activity on energization and loss of radiation belt electrons by oblique chorus waves. *J. Geophys. Res.*, **119**, 2775–2796.
- Mozer, F., Agapitov, O., Krasnoselskikh, V., Lejosne, S., Reeves, G., and Roth, I. (2014). Direct observation of radiation-belt electron acceleration from electron-volt energies to megavolts by nonlinear whistlers. *Physical review letters*, **113**(3), 035 001.
- Mozer, F. S., Agapitov, O. V., Artemyev, A., Drake, J. F., Krasnoselskikh, V., Lejosne, S., and Vasko, I. (2015). Time domain structures: What and where they are, what they do, and how they are made. *Geophys. Res. Lett.*, **42**, 3627–3638.
- Ni, B., Thorne, R. M., Meredith, N. P., Shprits, Y. Y., and Horne, R. B. (2011). Diffuse auroral scattering by whistler mode chorus waves: Dependence on wave normal angle distribution. *Journal of Geophysical Research (Space Physics)*, **116**, A10 207.
- Ni, B., Bortnik, J., Thorne, R. M., Ma, Q., and Chen, L. (2013). Resonant scattering and resultant pitch angle evolution of relativistic electrons by plasmaspheric hiss. *Journal of Geophysical Research (Space Physics)*, **118**, 7740–7751.

- Pokhotelov, D., Lefeuvre, F., Horne, R. B., and Cornilleau-Wehrin, N. (2008). Survey of ELF-VLF plasma waves in outer radiation belt observed by Cluster STAFF-SA experiment. *Ann. Geofis.*, **26**(11), 3269–3277.
- Reeves, G., Spence, H., Henderson, M., Morley, S., Friedel, R., Funsten, H., Baker, D., Kanekal, S., Blake, J., Fennell, J., Claudepierre, S., Thorne, R., Turner, D., Kletzing, C., Kurth, W., Larsen, B., and Niehof, J. (2013). Electron acceleration in the heart of the Van Allen radiation belts. *Science*, **341**, 991–994. ISSN 1095-9203.
- Sazhin, S. and Hayakawa, M. (1992). Magnetospheric chorus emissions: A review. *Planet. Space Sci.*, **40**(5), 681–697.
- Shprits, Y. Y. and Ni, B. (2009). Dependence of the quasi-linear scattering rates on the wave normal distribution of chorus waves. *Journal of Geophysical Research (Space Physics)*, **114**, A11 205.
- Shprits, Y. Y., Thorne, R. M., Horne, R. B., and Summers, D. (2006). Bounce-averaged diffusion coefficients for field-aligned chorus waves. *Journal of Geophysical Research (Space Physics)*, **111**, A10 225.
- SIA (2016). State of the Satellite Industry Report June 2016. <http://www.sia.org/wp-content/uploads/2016/06/SSIR16-Pdf-Copy-for-Website-Compressed.pdf>.
- Spasojevic, M. and Shprits, Y. Y. (2013). Chorus functional dependencies derived from crres data. *Geophys. Res. Lett.*, **40**, 3793–3797.
- Spasojevic, M., Shprits, Y. Y., and Orlova, K. (2015). Global empirical models of plasmaspheric hiss using van allen probes. *Journal of Geophysical Research (Space Physics)*, **120**, 10.
- Summers, D., Ni, B., and Meredith, N. P. (2007). Timescales for radiation belt electron acceleration and loss due to resonant wave-particle interactions: 1. Theory. *Journal of Geophysical Research (Space Physics)*, **112**, A04 206.

Thorne, R. M. (2010). Radiation belt dynamics: The importance of wave-particle interactions. *Geophys. Res. Lett.*, **33**(22), 22 107.

Thorne, R. M., Li, W., Ni, B., Ma, Q., Bortnik, J., Chen, L., Baker, D. N., Spence, H. E., Reeves, G. D., Henderson, M. G., Kletzing, C. A., Kurth, W. S., Hospodarsky, G. B., Blake, J. B., Fennell, J. F., Claudepierre, S. G., and Kanekal, S. G. (2013). Rapid local acceleration of relativistic radiation-belt electrons by magnetospheric chorus. *Nature*, **504**, 411–414.

Trakhtengerts, V. Y. (1966). Stationary states of the Earth’s outer radiation zone. *Geomagnetism and Aeronomy*, **6**, 827–836.

Tsurutani, B. T. and Smith, E. J. (1974). Postmidnight chorus: A substorm phenomenon. *J. Geophys. Res.*, **79**(1), 118–127.

Usanova, M. E., Drozdov, A., Orlova, K., Mann, I. R., Shprits, Y., Robertson, M. T., Turner, D. L., Milling, D. K., Kale, A., Baker, D. N., Thaller, S. A., Reeves, G. D., Spence, H. E., Kletzing, C., and Wygant, J. (2014). Effect of emic waves on relativistic and ultrarelativistic electron populations: Ground-based and van allen probes observations. *Geophys. Res. Lett.*, **41**, 1375–1381.

A LBC models

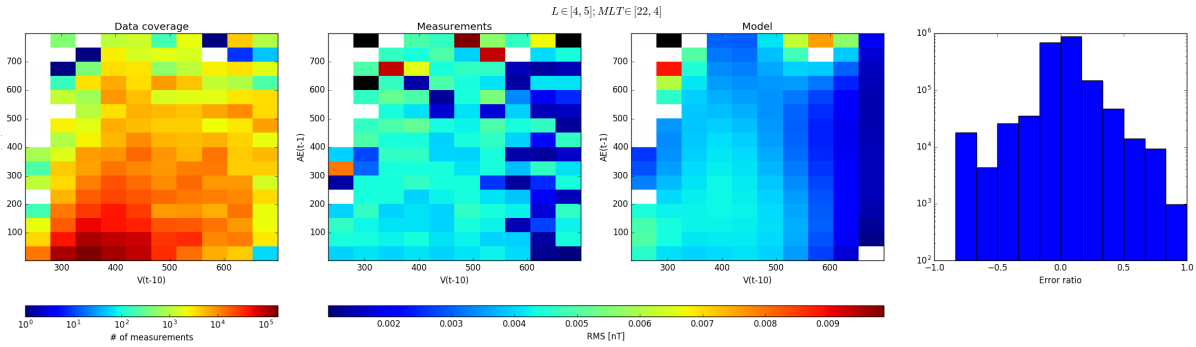


Figure 14: Data coverage, measured and analytical values of RMS of magnetic field amplitudes in V_{sw} -AE domain for region $4 < L \leq 5$ and 22:00-04:00 MLT in same format as Figure 2.

Table 2: Values of the coefficients a_{ij} for the model of RMS magnetic wave amplitudes B_w in V_{sw} -AE domain for region $4 < L \leq 5$ and 22:00-04:00 MLT.

i/j	0	1	2	3
0	-5.670e+00	2.219e-02	-4.695e-05	2.564e-08
1	3.082e-02	-2.208e-04	4.987e-07	-3.133e-10
2	-8.975e-05	6.672e-07	-1.546e-09	1.011e-12
3	8.105e-08	-6.182e-10	1.449e-12	-9.670e-16

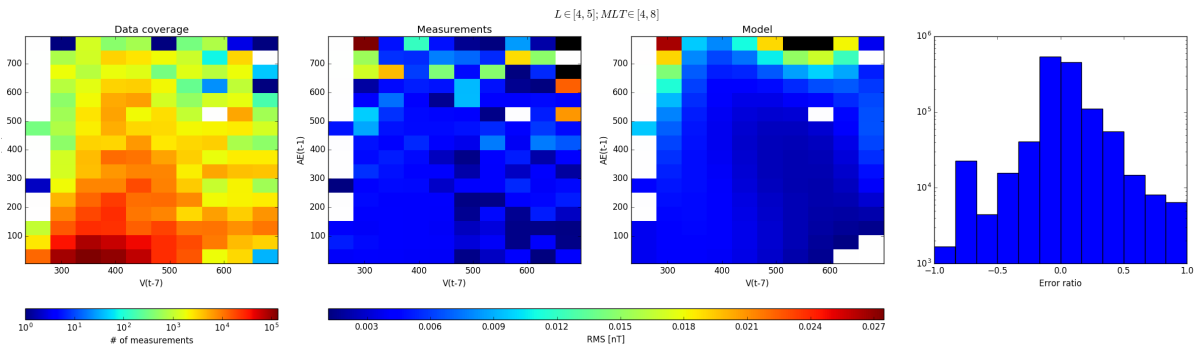


Figure 15: Data coverage, measured and analytical values of RMS of magnetic field amplitudes in V_{sw} -AE domain for region $4 < L \leq 5$ and 04:00-08:00 MLT in same format as Figure 2.

Table 3: Values of the coefficients a_{ij} for the model of RMS magnetic wave amplitudes B_w in V_{sw} -AE domain for region $4 < L \leq 5$ and 04:00-08:00 MLT.

i/j	0	1	2	3
0	-2.409e+00	-4.803e-03	9.049e-06	-1.102e-08
1	9.681e-04	2.499e-05	-3.621e-09	-3.864e-12
2	-7.700e-06	1.219e-08	-2.949e-10	3.242e-13
3	1.431e-08	-9.539e-11	5.193e-13	-5.162e-16

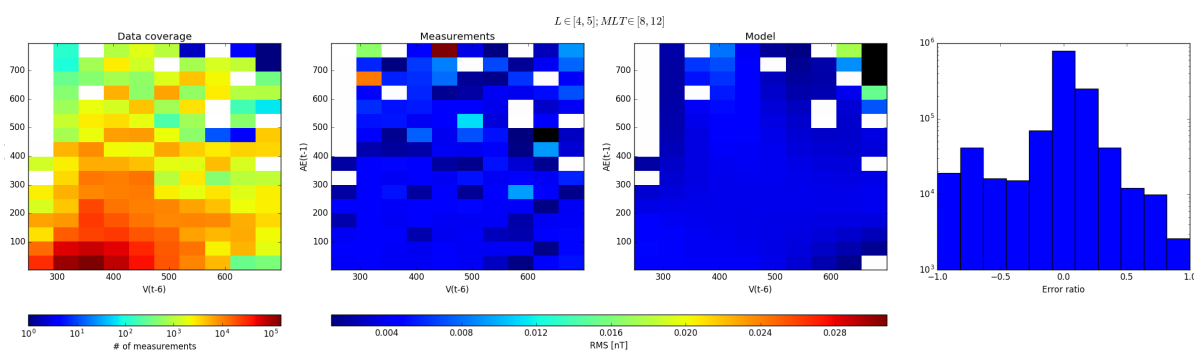


Figure 16: Data coverage, measured and analytical values of RMS of magnetic field amplitudes in V_{sw} -AE domain for region $4 < L \leq 5$ and 08:00-12:00 MLT in same format as Figure 2.

Table 4: Values of the coefficients a_{ij} for the model of RMS magnetic wave amplitudes B_w in V_{sw} -AE domain for region $4 < L \leq 5$ and 8:00-12:00 MLT.

i/j	0	1	2	3
0	-3.097e+00	-6.851e-03	6.254e-05	-9.027e-08
1	6.115e-03	5.675e-05	-4.949e-07	6.894e-10
2	-1.249e-05	-1.921e-07	1.372e-09	-1.791e-12
3	2.308e-09	2.425e-10	-1.335e-12	1.594e-15

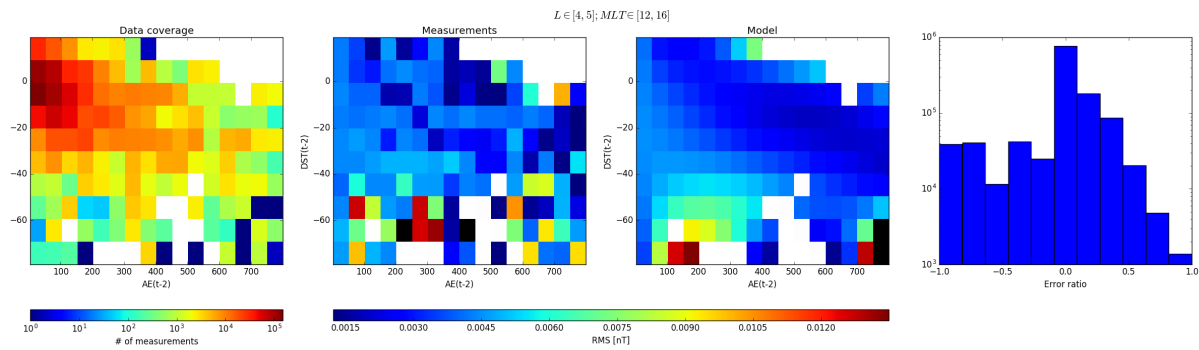


Figure 17: Data coverage, measured and analytical values of RMS of magnetic field amplitudes in AE-Dst domain for region $4 < L \leq 5$ and 12:00-16:00 MLT in same format as Figure 2.

Table 5: Values of the coefficients a_{ij} for the model of RMS magnetic wave amplitudes B_w in AE-Dst domain for region $4 < L \leq 5$ and 12:00-16:00 MLT.

i/j	0	1	2	3
0	-2.830e+00	4.498e-02	2.249e-03	2.049e-05
1	4.775e-03	-3.930e-04	-1.744e-05	-1.492e-07
2	-1.728e-05	9.327e-07	4.247e-08	3.549e-10
3	1.650e-08	-6.426e-10	-3.174e-11	-2.661e-13

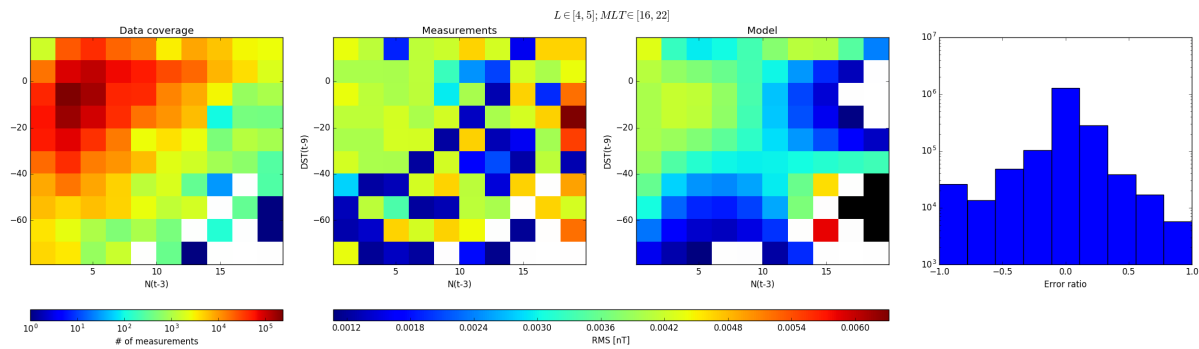


Figure 18: Data coverage, measured and analytical values of RMS of magnetic field amplitudes in N-Dst domain for region $4 < L \leq 5$ and 16:00-22:00 MLT in same format as Figure 2.

Table 6: Values of the coefficients a_{ij} for the model of RMS magnetic wave amplitudes B_w in N-Dst domain for region $4 < L \leq 5$ and 16:00-22:00 MLT.

i/j	0	1	2	3
0	-2.310e+00	3.858e-02	6.347e-04	2.867e-06
1	1.184e-01	-2.490e-03	-1.330e-04	-1.232e-06
2	-2.338e-02	-3.606e-04	8.916e-06	1.372e-07
3	8.640e-04	1.893e-05	-2.308e-07	-4.546e-09

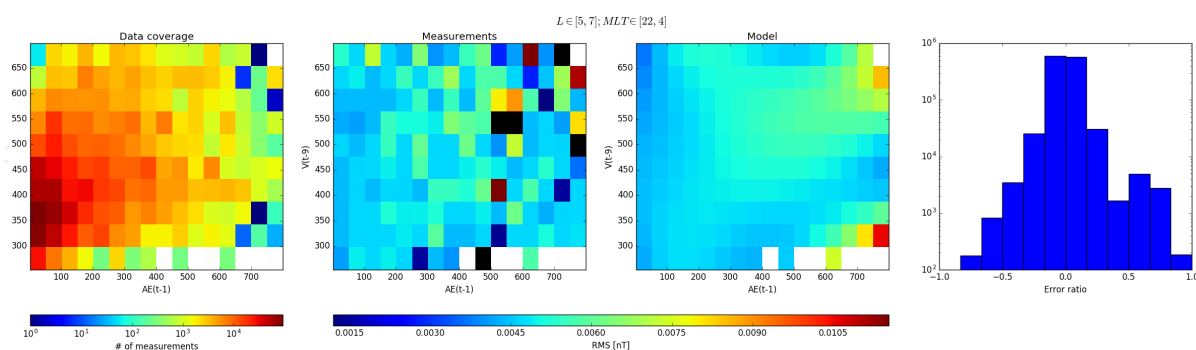


Figure 19: Data coverage, measured and analytical values of RMS of magnetic field amplitudes in AE- V_{sw} domain for region $5 < L < 7$ and 22:00-04:00 MLT in same format as Figure 2.

Table 7: Values of the coefficients a_{ij} for the model of RMS magnetic wave amplitudes B_w in AE- V_{sw} domain for region $5 < L < 7$ and 22:00-04:00 MLT.

i/j	0	1	2	3
0	-4.265e+00	1.551e-02	-4.031e-05	3.384e-08
1	8.304e-03	-7.054e-05	1.967e-07	-1.775e-10
2	-5.895e-06	5.512e-08	-1.821e-10	1.988e-13
3	-6.495e-09	4.423e-11	-7.633e-14	1.811e-17

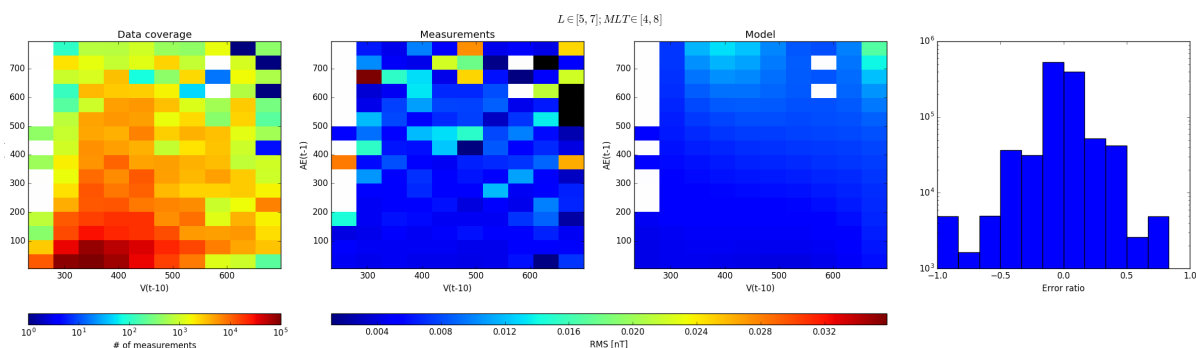


Figure 20: Data coverage, measured and analytical values of RMS of magnetic field amplitudes in V_{sw} -AE domain for region $5 < L < 7$ and 04:00-08:00 MLT in same format as Figure 2.

Table 8: Values of the coefficients a_{ij} for the model of RMS magnetic wave amplitudes B_w in V_{sw} -AE domain for region $5 < L < 7$ and 04:00-08:00 MLT.

i/j	0	1	2	3
0	-2.065e+00	-3.297e-03	6.883e-06	-4.641e-09
1	-3.360e-03	3.731e-05	-9.704e-08	7.647e-11
2	1.128e-05	-1.192e-07	3.357e-10	-2.723e-13
3	-1.066e-08	1.207e-10	-3.471e-13	2.814e-16

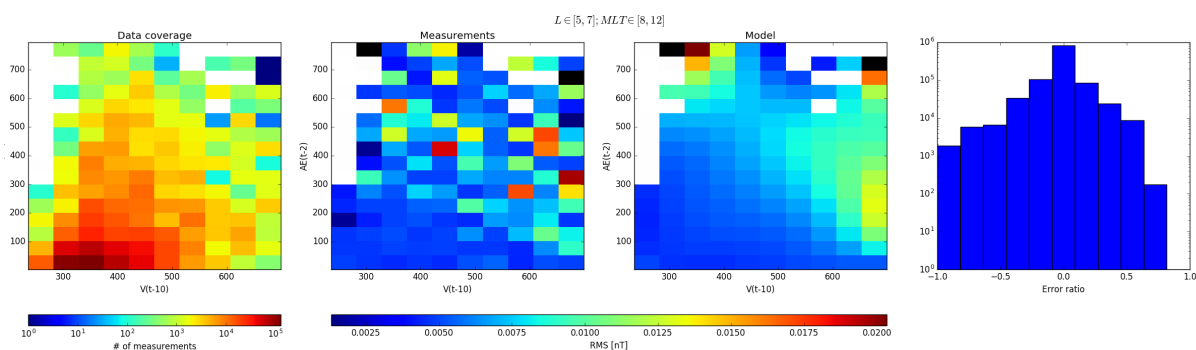


Figure 21: Data coverage, measured and analytical values of RMS of magnetic field amplitudes in V_{sw} -AE domain for region $5 < L < 7$ and 08:00-12:00 MLT in same format as Figure 2.

Table 9: Values of the coefficients a_{ij} for the model of RMS magnetic wave amplitudes B_w in V_{sw} -AE domain for region $5 < L < 7$ and 08:00-12:00 MLT.

i/j	0	1	2	3
0	-1.263e+00	-2.183e-02	8.018e-05	-7.790e-08
1	-7.900e-03	1.729e-04	-6.543e-07	6.390e-10
2	1.731e-05	-4.280e-07	1.681e-09	-1.642e-12
3	-1.067e-08	3.380e-10	-1.374e-12	1.342e-15

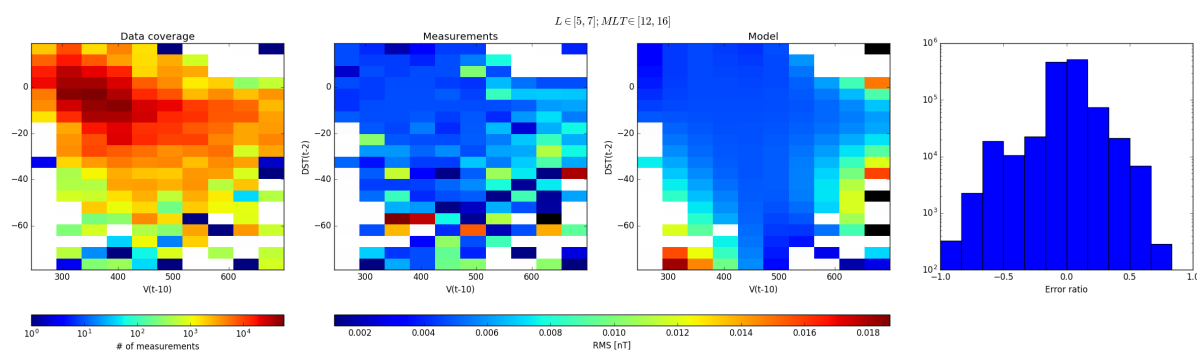


Figure 22: Data coverage, measured and analytical values of RMS of magnetic field amplitudes in V_{sw} -Dst domain for region $5 < L < 7$ and 12:00-16:00 MLT in same format as Figure 2.

Table 10: Values of the coefficients a_{ij} for the model of RMS magnetic wave amplitudes B_w in V_{sw} -Dst domain for region $5 < L < 7$ and 12:00-16:00 MLT.

i/j	0	1	2	3
0	-9.670e+00	-3.248e-01	-2.924e-03	-5.795e-07
1	5.045e-02	2.479e-03	3.041e-05	8.383e-08
2	-1.093e-04	-5.774e-06	-8.256e-08	-3.192e-10
3	7.645e-08	4.269e-09	6.737e-11	3.074e-13

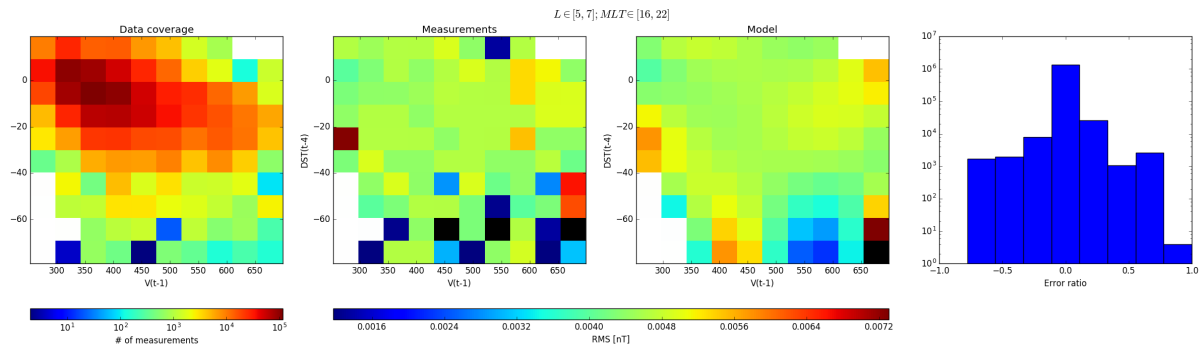


Figure 23: Data coverage, measured and analytical values of RMS of magnetic field amplitudes in V_{sw} -Dst domain for region $5 < L < 7$ and 16:00-22:00 MLT in same format as Figure 2.

Table 11: Values of the coefficients a_{ij} for the model of RMS magnetic wave amplitudes B_w in V_{sw} -Dst domain for region $5 < L < 7$ and 16:00-22:00 MLT.

i/j	0	1	2	3
0	-3.535e+00	7.227e-02	6.652e-03	9.472e-05
1	4.989e-03	-3.980e-04	-3.439e-05	-4.966e-07
2	-6.136e-06	7.053e-07	5.738e-08	8.430e-10
3	2.052e-09	-3.997e-10	-3.087e-11	-4.640e-13

B Hiss models

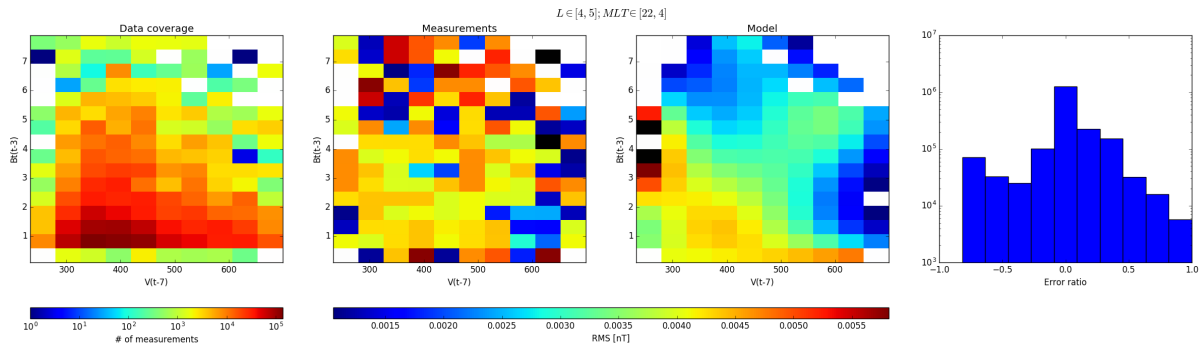


Figure 24: Data coverage, measured and analytical values of RMS of magnetic field amplitudes in V_{sw} -Bt domain for region $4 < L \leq 5$ and 22:00-04:00 MLT in same format as Figure 2.

Table 12: Values of the coefficients a_{ij} for the model of RMS magnetic wave amplitudes B_w in V_{sw} -Bt domain for region $4 < L \leq 5$ and 22:00-04:00 MLT.

i/j	0	1	2	3
0	1.617e+00	-3.991e+00	9.089e-01	-4.076e-02
1	-3.583e-02	3.503e-02	-7.965e-03	3.763e-04
2	1.001e-04	-9.525e-05	2.160e-05	-1.075e-06
3	-8.700e-08	7.954e-08	-1.791e-08	9.170e-10

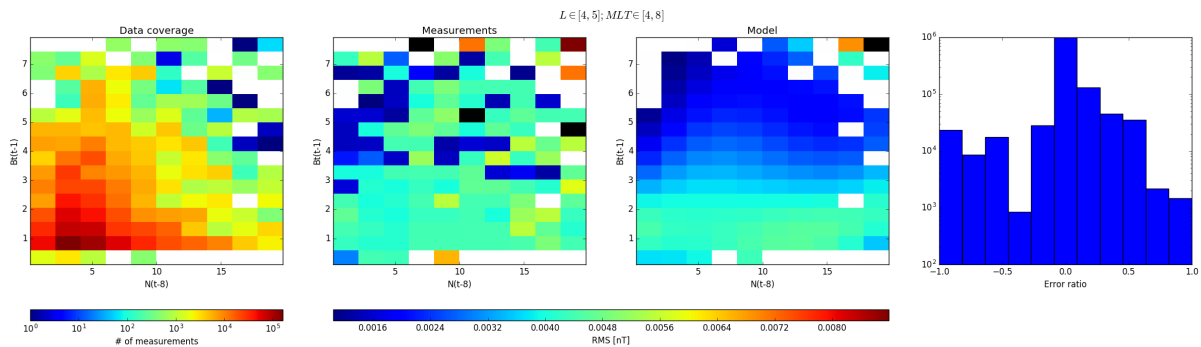


Figure 25: Data coverage, measured and analytical values of RMS of magnetic field amplitudes in N-Bt domain for region $4 < L \leq 5$ and 04:00-08:00 MLT in same format as Figure 2.

Table 13: Values of the coefficients a_{ij} for the model of RMS magnetic wave amplitudes B_w in N-Bt domain for region $4 < L \leq 5$ and 04:00-08:00 MLT.

i/j	0	1	2	3
0	-2.440e+00	-2.914e-03	1.342e-02	-1.940e-03
1	6.751e-02	-2.980e-02	4.210e-03	3.908e-05
2	-1.375e-02	7.411e-03	-1.727e-03	9.133e-05
3	4.411e-04	-2.857e-04	7.505e-05	-4.419e-06

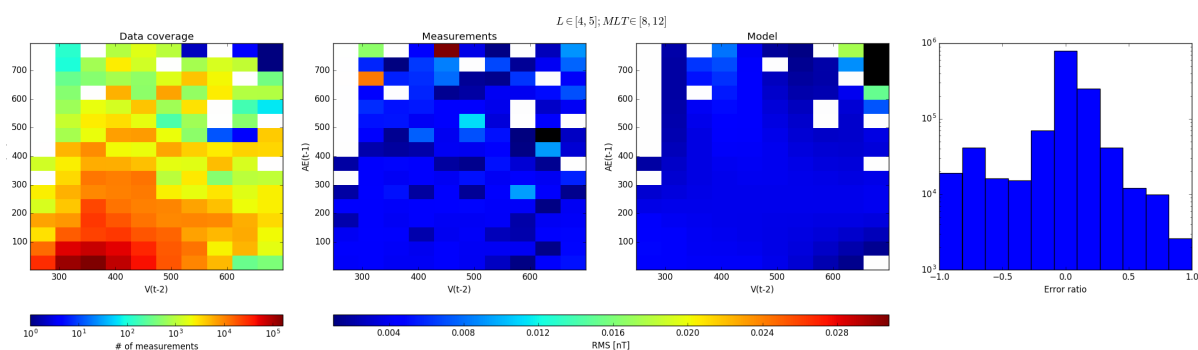


Figure 26: Data coverage, measured and analytical values of RMS of magnetic field amplitudes in V_{sw} -AE domain for region $4 < L \leq 5$ and 08:00-12:00 MLT in same format as Figure 2.

Table 14: Values of the coefficients a_{ij} for the model of RMS magnetic wave amplitudes B_w in V_{sw} -AE domain for region $4 < L \leq 5$ and 08:00-12:00 MLT.

i/j	0	1	2	3
0	-3.097e+00	-6.851e-03	6.254e-05	-9.027e-08
1	6.115e-03	5.675e-05	-4.949e-07	6.894e-10
2	-1.249e-05	-1.921e-07	1.372e-09	-1.791e-12
3	2.308e-09	2.425e-10	-1.335e-12	1.594e-15

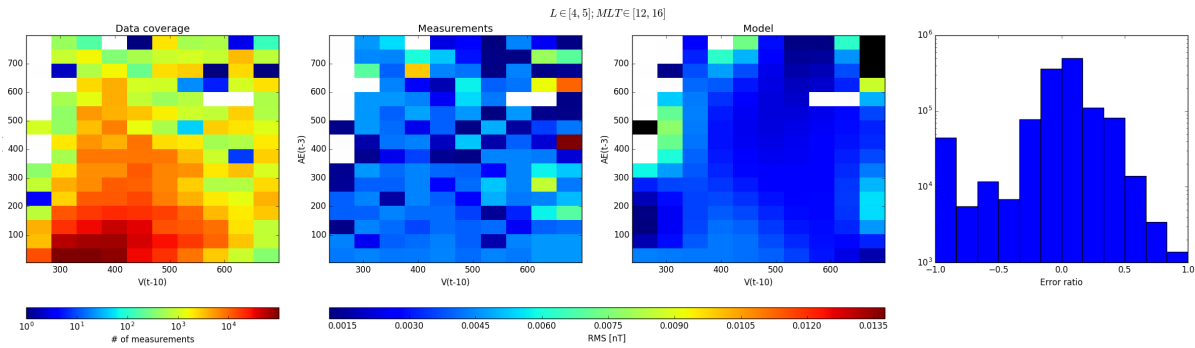


Figure 27: Data coverage, measured and analytical values of RMS of magnetic field amplitudes in V_{sw} -AE domain for region $4 < L \leq 5$ and 12:00-16:00 MLT in same format as Figure 2.

Table 15: Values of the coefficients a_{ij} for the model of RMS magnetic wave amplitudes B_w in V_{sw} -AE domain for region $4 < L \leq 5$ and 12:00-16:00 MLT.

i/j	0	1	2	3
0	1.503e+01	-1.439e-01	3.557e-04	-2.710e-07
1	-1.454e-01	1.204e-03	-2.952e-06	2.223e-09
2	3.768e-04	-3.128e-06	7.616e-09	-5.685e-12
3	-3.062e-07	2.554e-09	-6.204e-12	4.611e-15

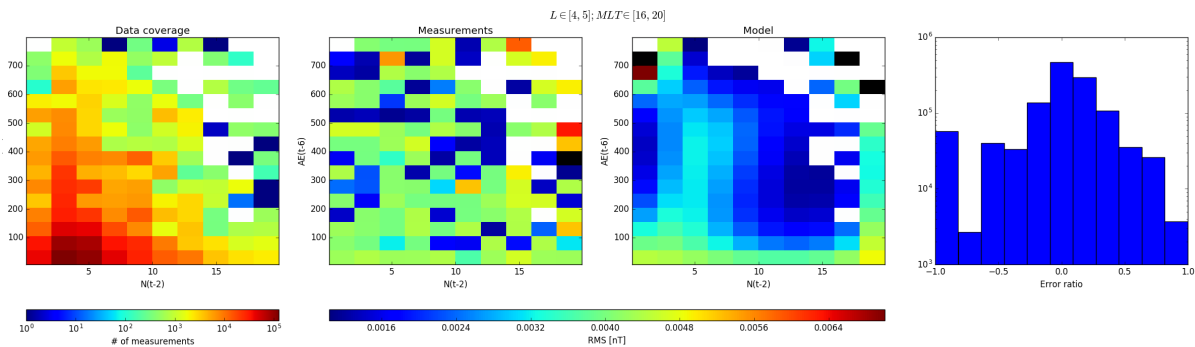


Figure 28: Data coverage, measured and analytical values of RMS of magnetic field amplitudes in N-AE domain for region $4 < L \leq 5$ and 16:00-20:00 MLT in same format as Figure 2.

Table 16: Values of the coefficients a_{ij} for the model of RMS magnetic wave amplitudes B_w in N-AE domain for region $4 < L \leq 5$ and 16:00-20:00 MLT.

i/j	0	1	2	3
0	-2.347e+00	-2.819e-05	-7.097e-07	1.002e-09
1	-3.305e-02	1.927e-04	-2.135e-06	2.401e-09
2	-8.525e-03	9.571e-05	-3.164e-08	-9.990e-11
3	6.480e-04	-7.015e-06	1.023e-08	-2.449e-12

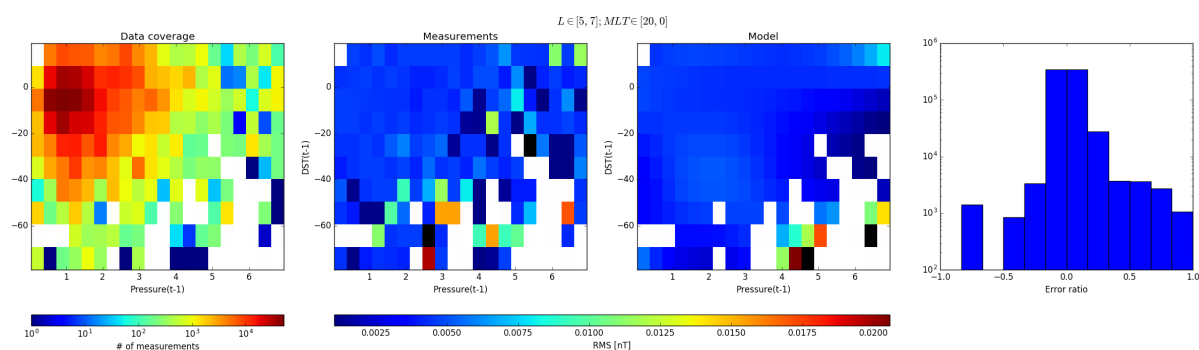


Figure 29: Data coverage, measured and analytical values of RMS of magnetic field amplitudes in P-Dst domain for region $5 < L < 7$ and 20:00-00:00 MLT in same format as Figure 2.

Table 17: Values of the coefficients a_{ij} for the model of RMS magnetic wave amplitudes B_w in P-Dst domain for region $5 < L < 7$ and 20:00-00:00 MLT.

i/j	0	1	2	3
0	-4.175e-01	8.954e-02	1.037e-03	2.481e-06
1	-1.600e+00	-6.973e-02	-5.916e-04	9.907e-07
2	3.415e-01	1.408e-02	7.537e-05	-7.857e-07
3	-2.161e-02	-8.299e-04	-1.097e-06	9.009e-08

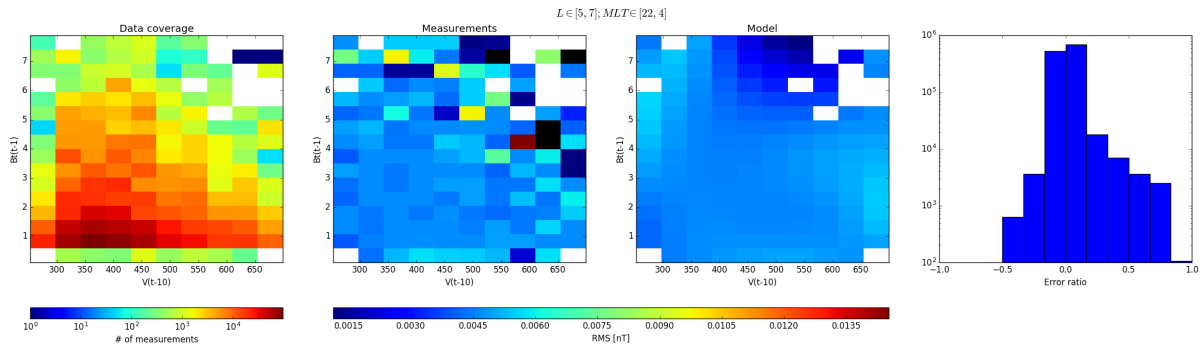


Figure 30: Data coverage, measured and analytical values of RMS of magnetic field amplitudes in V_{sw} -Bt domain for region $5 < L < 7$ and 22:00-04:00 MLT in same format as Figure 2.

Table 18: Values of the coefficients a_{ij} for the model of RMS magnetic wave amplitudes B_w in V_{sw} -Bt domain for region $5 < L < 7$ and 22:00-04:00 MLT.

i/j	0	1	2	3
0	-1.631e+00	-1.117e+00	4.723e-01	-4.569e-02
1	-6.319e-03	9.604e-03	-3.913e-03	3.714e-04
2	1.661e-05	-2.522e-05	1.015e-05	-9.512e-07
3	-1.303e-08	2.044e-08	-8.305e-09	7.756e-10

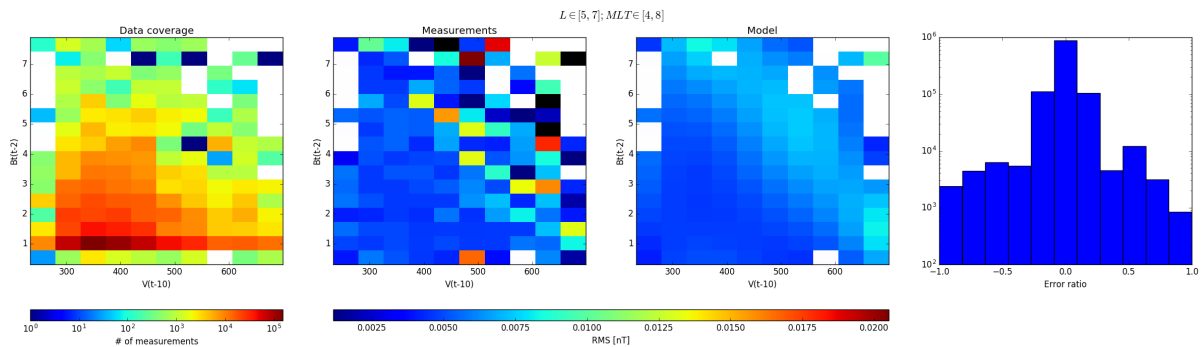


Figure 31: Data coverage, measured and analytical values of RMS of magnetic field amplitudes in V_{sw} -Bt domain for region $5 < L < 7$ and 04:00-08:00 MLT in same format as Figure 2.

Table 19: Values of the coefficients a_{ij} for the model of RMS magnetic wave amplitudes B_w in V_{sw} -Bt domain for region $5 < L < 7$ and 04:00-08:00 MLT.

i/j	0	1	2	3
0	-2.680e+00	3.638e-01	5.504e-04	-1.044e-02
1	6.560e-04	3.025e-04	-1.083e-03	1.783e-04
2	3.258e-06	-8.281e-06	5.196e-06	-6.554e-07
3	-5.322e-09	1.134e-08	-5.606e-09	6.377e-10

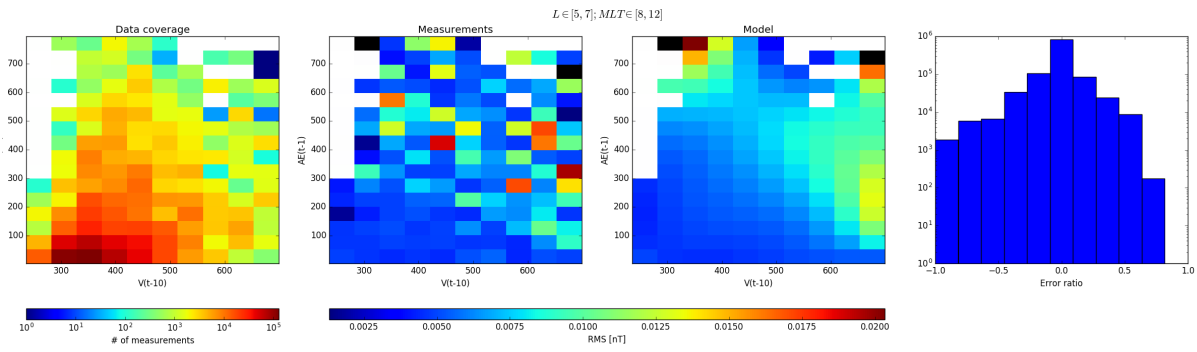


Figure 32: Data coverage, measured and analytical values of RMS of magnetic field amplitudes in V_{sw} -AE domain for region $5 < L < 7$ and 08:00-12:00 MLT in same format as Figure 2.

Table 20: Values of the coefficients a_{ij} for the model of RMS magnetic wave amplitudes B_w in V_{sw} -AE domain for region $5 < L < 7$ and 08:00-12:00 MLT.

i/j	0	1	2	3
0	-1.263e+00	-2.183e-02	8.018e-05	-7.790e-08
1	-7.900e-03	1.729e-04	-6.543e-07	6.390e-10
2	1.731e-05	-4.280e-07	1.681e-09	-1.642e-12
3	-1.067e-08	3.380e-10	-1.374e-12	1.342e-15

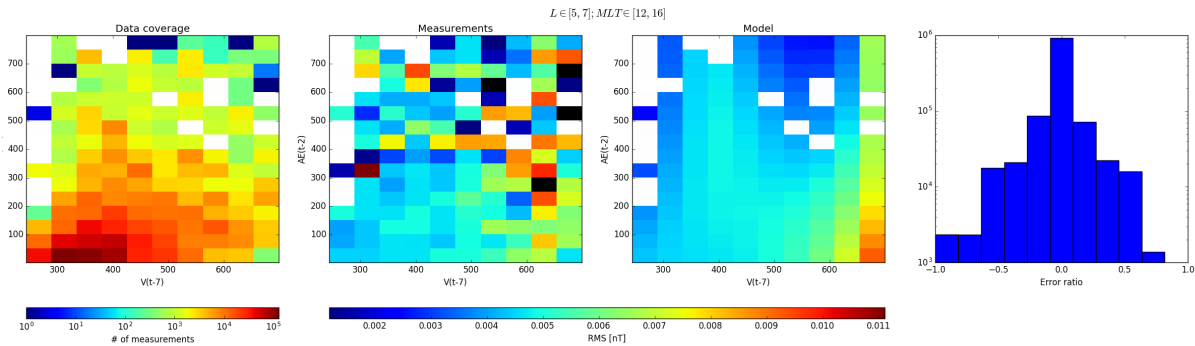


Figure 33: Data coverage, measured and analytical values of RMS of magnetic field amplitudes in V_{sw} -AE domain for region $5 < L < 7$ and 12:00-16:00 MLT in same format as Figure 2.

Table 21: Values of the coefficients a_{ij} for the model of RMS magnetic wave amplitudes B_w in V_{sw} -AE domain for region $5 < L < 7$ and 12:00-16:00 MLT.

i/j	0	1	2	3
0	-2.596e+00	1.991e-03	-5.888e-06	5.936e-09
1	2.430e-03	-1.914e-05	5.152e-08	-4.231e-11
2	-7.220e-06	5.908e-08	-1.495e-10	1.115e-13
3	4.757e-09	-3.744e-11	8.381e-14	-5.587e-17

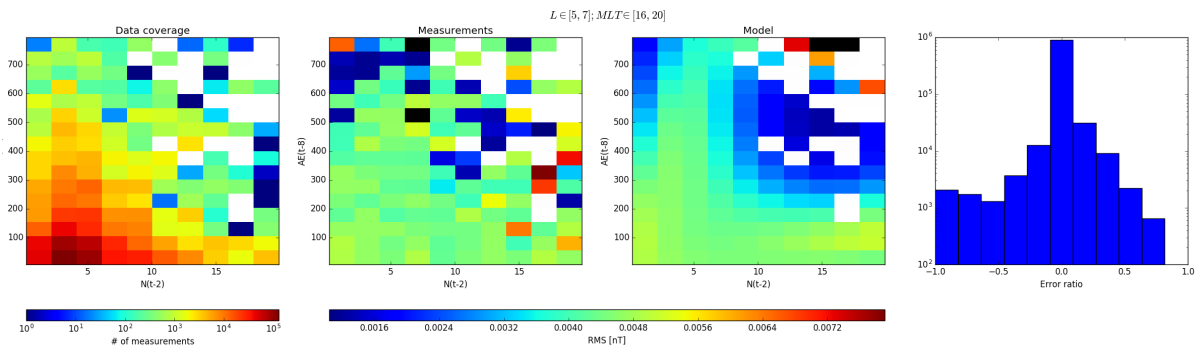


Figure 34: Data coverage, measured and analytical values of RMS of magnetic field amplitudes in N-AE domain for region $5 < L < 7$ and 16:00-20:00 MLT in same format as Figure 2.

Table 22: Values of the coefficients a_{ij} for the model of RMS magnetic wave amplitudes B_w in N-AE domain for region $5 < L < 7$ and 16:00-20:00 MLT.

i/j	0	1	2	3
0	-2.307e+00	-3.187e-04	7.504e-07	-5.666e-10
1	5.162e-03	-1.302e-04	4.755e-07	-2.311e-10
2	-1.920e-03	4.379e-05	-1.942e-07	1.295e-10
3	2.928e-05	-1.431e-06	7.111e-09	-4.221e-12

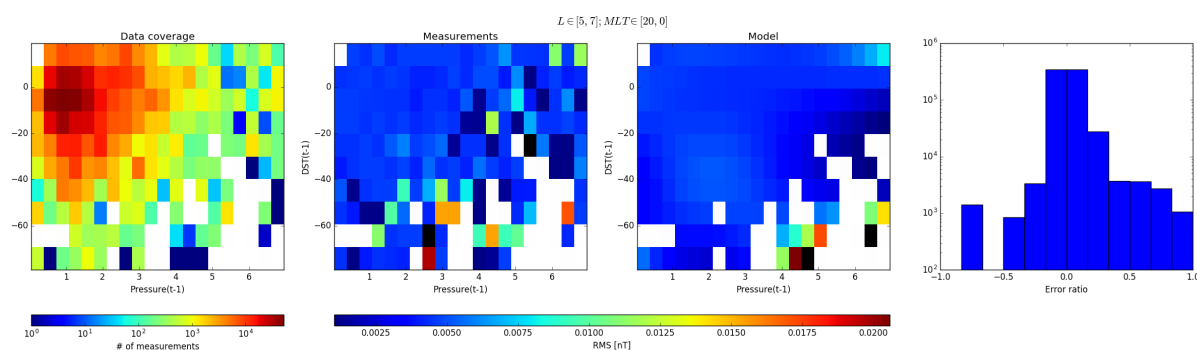


Figure 35: Data coverage, measured and analytical values of RMS of magnetic field amplitudes in P-Dst domain for region $5 < L < 7$ and 20:00-00:00 MLT in same format as Figure 2.

Table 23: Values of the coefficients a_{ij} for the model of RMS magnetic wave amplitudes B_w in P-Dst domain for region $5 < L < 7$ and 20:00-00:00 MLT.

i/j	0	1	2	3
0	-4.175e-01	8.954e-02	1.037e-03	2.481e-06
1	-1.600e+00	-6.973e-02	-5.916e-04	9.907e-07
2	3.415e-01	1.408e-02	7.537e-05	-7.857e-07
3	-2.161e-02	-8.299e-04	-1.097e-06	9.009e-08

C EMW models

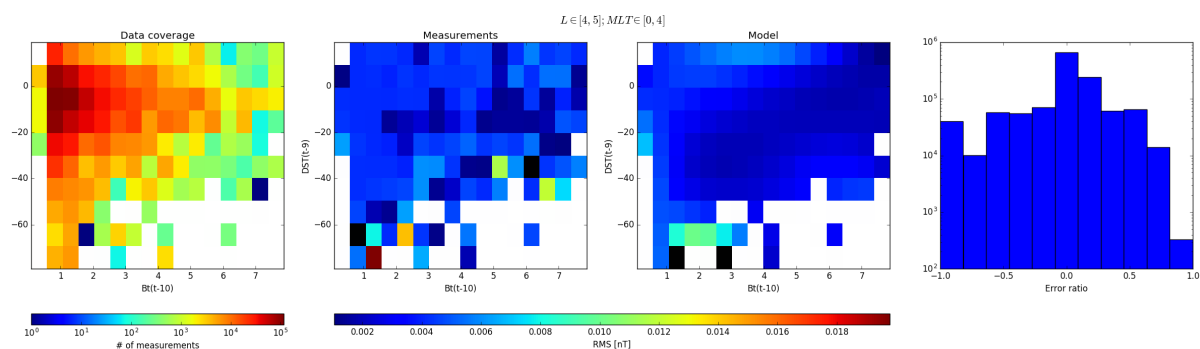


Figure 36: Data coverage, measured and analytical values of RMS of magnetic field amplitudes in Bt-Dst domain for region $4 < L \leq 5$ and 00:00-04:00 MLT in same format as Figure 2.

Table 24: Values of the coefficients a_{ij} for the model of RMS magnetic wave amplitudes B_w in Bt-Dst domain for region $4 < L \leq 5$ and 00:00-04:00 MLT.

i/j	0	1	2	3
0	-2.798e+00	7.446e-02	4.098e-03	4.100e-05
1	4.444e-01	-4.744e-02	-3.028e-03	-3.154e-05
2	-1.381e-01	9.954e-03	6.548e-04	6.781e-06
3	1.096e-02	-6.889e-04	-4.340e-05	-4.395e-07

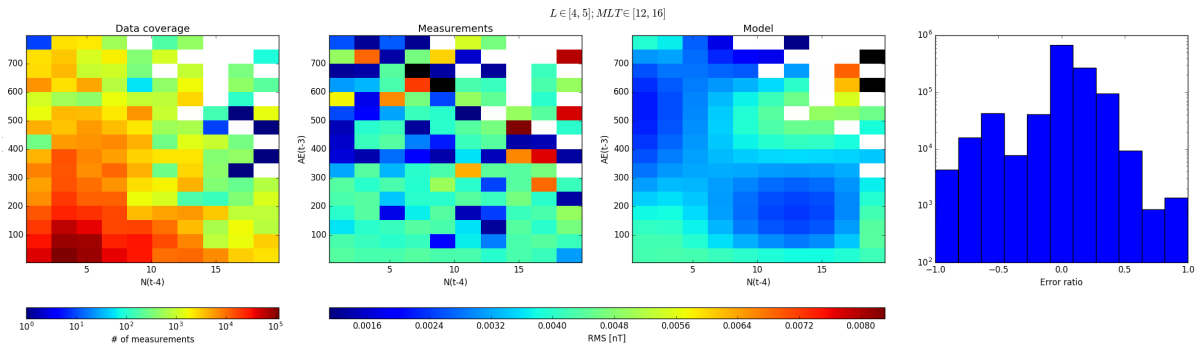


Figure 37: Data coverage, measured and analytical values of RMS of magnetic field amplitudes in N-AE domain for region $4 < L \leq 5$ and 12:00-16:00 MLT in same format as Figure 2.

Table 25: Values of the coefficients a_{ij} for the model of RMS magnetic wave amplitudes B_w in N-AE domain for region $4 < L \leq 5$ and 12:00-16:00 MLT.

i/j	0	1	2	3
0	-2.376e+00	1.107e-04	-3.438e-07	2.301e-10
1	9.563e-03	3.998e-05	-1.664e-06	2.068e-09
2	-5.993e-03	3.462e-06	2.745e-07	-3.562e-10
3	2.734e-04	-2.072e-07	-1.100e-08	1.465e-11

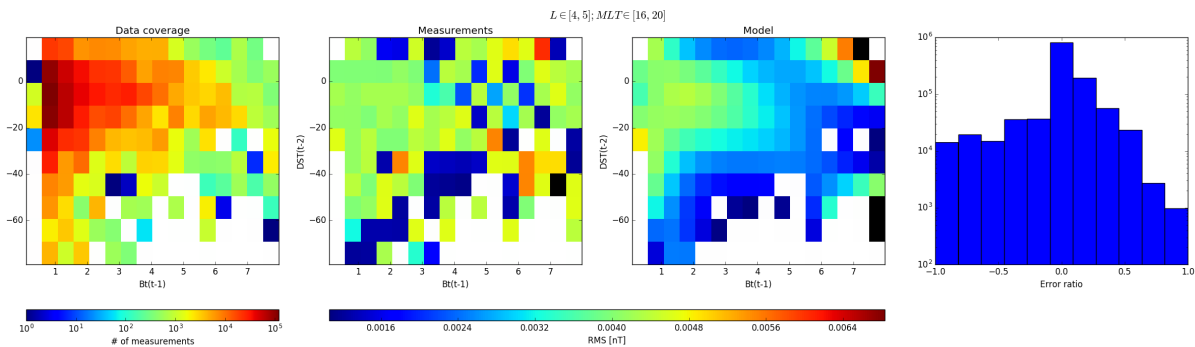


Figure 38: Data coverage, measured and analytical values of RMS of magnetic field amplitudes in Bt-Dst domain for region $4 < L \leq 5$ and 16:00-20:00 MLT in same format as Figure 2.

Table 26: Values of the coefficients a_{ij} for the model of RMS magnetic wave amplitudes B_w in Bt-Dst domain for region $4 < L \leq 5$ and 16:00-20:00 MLT.

i/j	0	1	2	3
0	-2.007e+00	1.775e-01	5.243e-03	4.076e-05
1	-3.078e-01	-1.049e-01	-3.469e-03	-2.942e-05
2	3.735e-02	1.851e-02	6.910e-04	6.245e-06
3	-4.964e-04	-9.960e-04	-4.221e-05	-4.024e-07

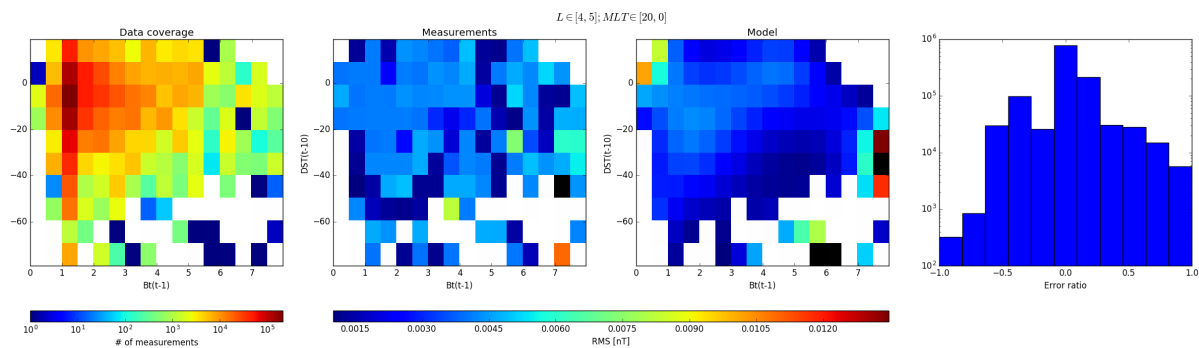


Figure 39: Data coverage, measured and analytical values of RMS of magnetic field amplitudes in Bt-Dst domain for region $4 < L \leq 5$ and 20:00-00:00 MLT in same format as Figure 2.

Table 27: Values of the coefficients a_{ij} for the model of RMS magnetic wave amplitudes B_w in Bt-Dst domain for region $4 < L \leq 5$ and 20:00-00:00 MLT.

i/j	0	1	2	3
0	-1.344e+00	-3.385e-02	-2.983e-03	-3.208e-05
1	-1.047e+00	3.555e-02	2.338e-03	2.304e-05
2	2.517e-01	-5.227e-03	-3.781e-04	-3.606e-06
3	-1.893e-02	3.999e-06	1.168e-05	1.100e-07

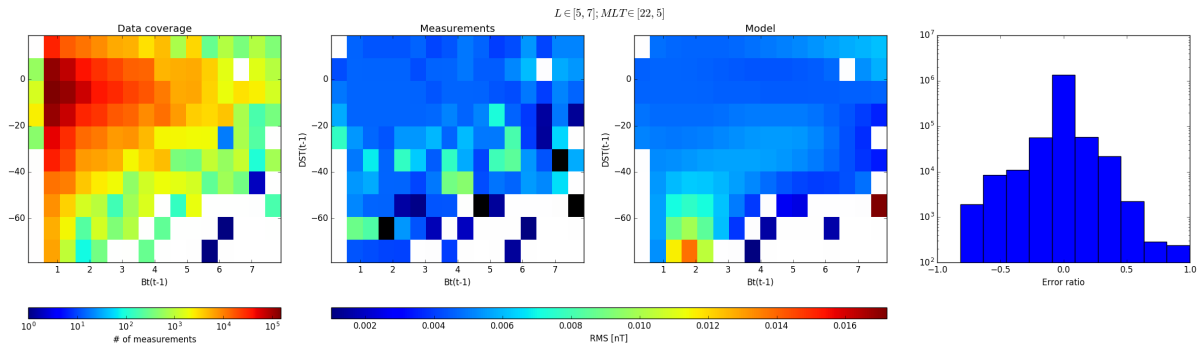


Figure 40: Data coverage, measured and analytical values of RMS of magnetic field amplitudes in Bt-Dst domain for region $5 < L < 7$ and 22:00-05:00 MLT in same format as Figure 2.

Table 28: Values of the coefficients a_{ij} for the model of RMS magnetic wave amplitudes B_w in Bt-Dst domain for region $5 < L < 7$ and 22:00-05:00 MLT.

i/j	0	1	2	3
0	-3.179e+00	9.193e-02	4.141e-03	3.727e-05
1	5.273e-01	-5.796e-02	-2.487e-03	-2.200e-05
2	-1.051e-01	1.087e-02	4.602e-04	4.046e-06
3	6.739e-03	-6.301e-04	-2.682e-05	-2.359e-07

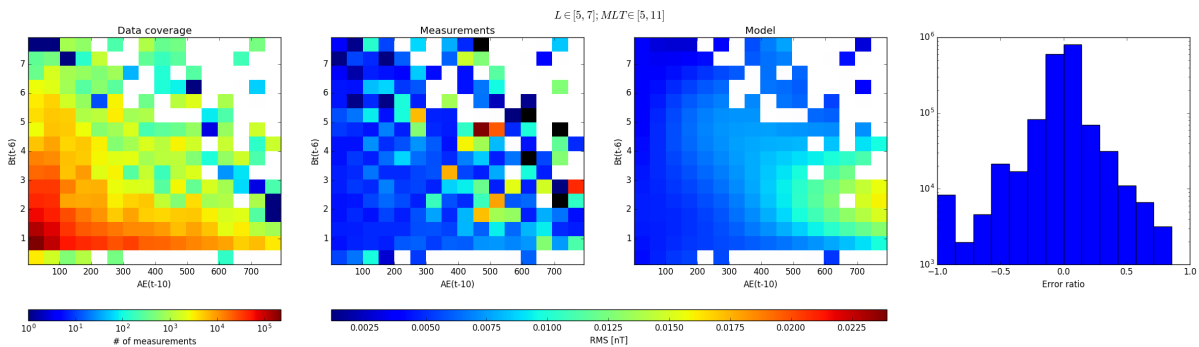


Figure 41: Data coverage, measured and analytical values of RMS of magnetic field amplitudes in AE-Bt domain for region $5 < L < 7$ and 05:00-11:00 MLT in same format as Figure 2.

Table 29: Values of the coefficients a_{ij} for the model of RMS magnetic wave amplitudes B_w in AE-Bt domain for region $5 < L < 7$ and 05:00-11:00 MLT.

i/j	0	1	2	3
0	-2.396e+00	1.395e-01	-4.121e-02	3.396e-03
1	7.862e-04	-2.030e-03	7.972e-04	-6.220e-05
2	-2.844e-06	8.374e-06	-3.078e-06	2.396e-07
3	2.329e-09	-8.149e-09	2.961e-09	-2.367e-10

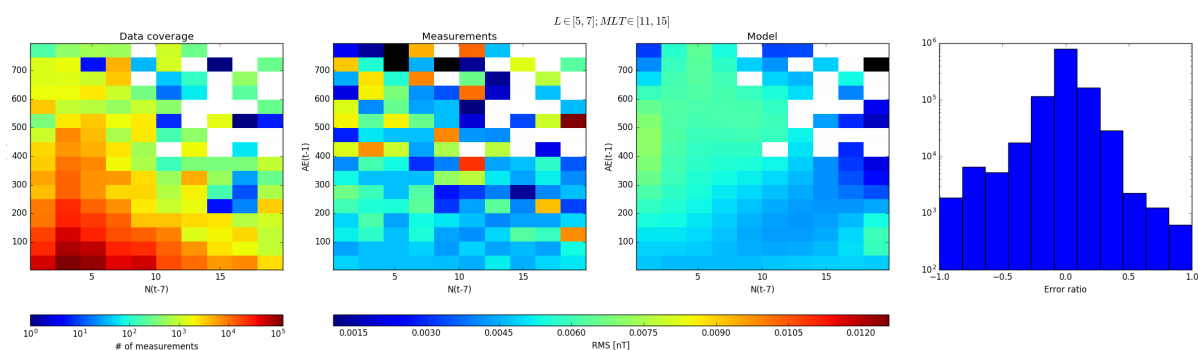


Figure 42: Data coverage, measured and analytical values of RMS of magnetic field amplitudes in N-AE domain for region $5 < L < 7$ and 11:00-15:00 MLT in same format as Figure 2.

Table 30: Values of the coefficients a_{ij} for the model of RMS magnetic wave amplitudes B_w in N-AE domain for region $5 < L < 7$ and 11:00-15:00 MLT.

i/j	0	1	2	3
0	-2.321e+00	-2.322e-04	9.111e-07	-8.075e-10
1	2.825e-03	3.115e-04	-1.734e-06	1.894e-09
2	3.452e-03	-7.294e-05	3.543e-07	-3.905e-10
3	-2.054e-04	3.474e-06	-1.583e-08	1.729e-11

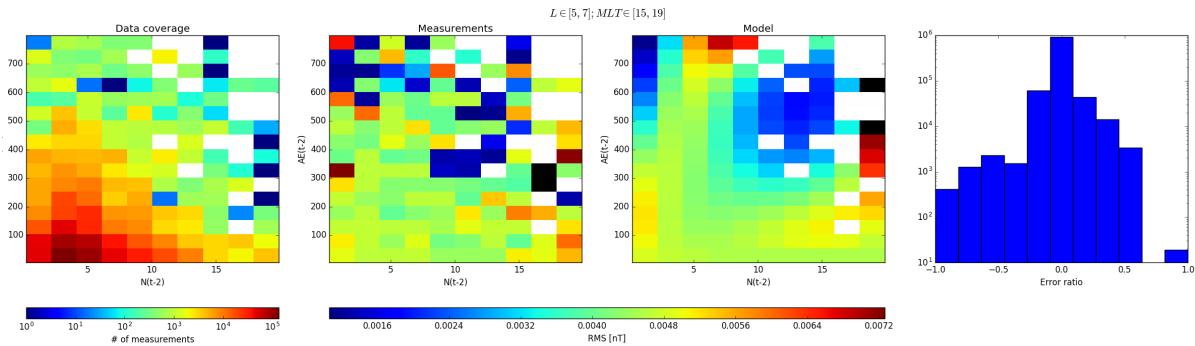


Figure 43: Data coverage, measured and analytical values of RMS of magnetic field amplitudes in N-AE domain for region $5 < L < 7$ and 15:00-19:00 MLT in same format as Figure 2.

Table 31: Values of the coefficients a_{ij} for the model of RMS magnetic wave amplitudes B_w in N-AE domain for region $5 < L < 7$ and 15:00-19:00 MLT.

i/j	0	1	2	3
0	-2.318e+00	-8.320e-05	-1.809e-08	9.691e-11
1	1.978e-02	-4.080e-04	1.587e-06	-1.366e-09
2	-2.582e-03	6.580e-05	-3.200e-07	3.064e-10
3	-3.836e-06	-1.428e-06	9.994e-09	-1.048e-11

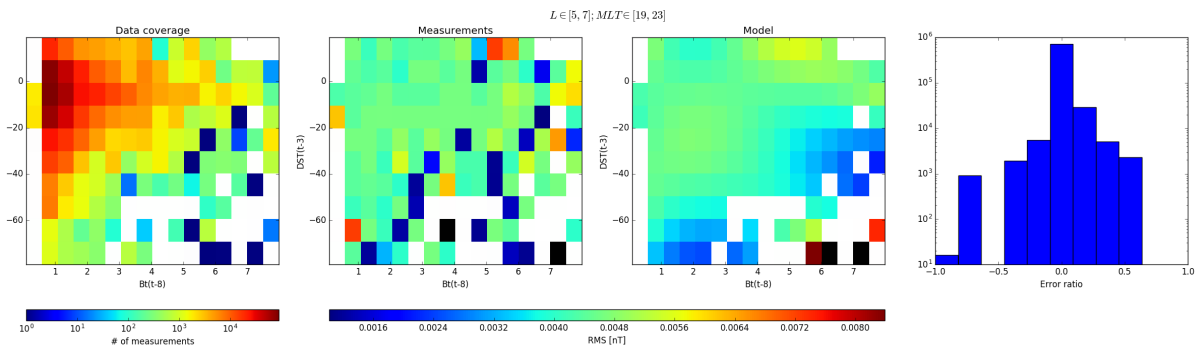


Figure 44: Data coverage, measured and analytical values of RMS of magnetic field amplitudes in Bt-Dst domain for region $5 < L < 7$ and 19:00-23:00 MLT in same format as Figure 2.

Table 32: Values of the coefficients a_{ij} for the model of RMS magnetic wave amplitudes B_w in Bt-Dst domain for region $5 < L < 7$ and 19:00-23:00 MLT.

i/j	0	1	2	3
0	-1.861e+00	2.782e-02	2.229e-04	-5.819e-07
1	-4.708e-01	-2.796e-02	-3.931e-04	-1.598e-06
2	1.020e-01	6.931e-03	1.274e-04	7.645e-07
3	-6.279e-03	-5.018e-04	-1.102e-05	-7.701e-08

D Models with simplified dependence on K_P

Table 33: Values of the coefficients a_{ij} for the model of the obliquity parameter of LBC waves B_w in λ - K_P domain for region $2 < L < 6$ and 03 : 00–15 : 00 MLT.

i/j	0	1	2	3
0	1.613e-02	-1.343e-02	3.497e-03	-2.766e-04
1	3.051e-02	-3.199e-02	1.050e-02	-9.992e-04
2	-5.596e-02	5.255e-02	-1.531e-02	1.318e-03
3	2.028e-02	-1.794e-02	4.905e-03	-3.958e-04

Table 34: Values of the coefficients b_k for the model of the obliquity parameter of LBC waves B_w in λ - K_P domain for region $2 < L < 6$ and 03 : 00–15 : 00 MLT.

i	0	1	2	3
	5.926e+00	1.643e+01	3.666e+00	-9.124e-01

Table 35: Values of the coefficients a_{ij} for the model of the obliquity parameter of LBC waves B_w in λ - K_P domain for region $2 < L < 6$ and 15 : 00–03 : 00 MLT.

i/j	0	1	2	3
0	2.490e-03	-2.252e-03	7.417e-04	-5.463e-05
1	5.711e-02	-6.312e-02	2.142e-02	-2.152e-03
2	-1.171e-01	1.217e-01	-3.868e-02	3.694e-03
3	4.599e-02	-4.620e-02	1.424e-02	-1.328e-03

Table 36: Values of the coefficients b_k for the model of the obliquity parameter of LBC waves B_w in λ - K_P domain for region $2 < L < 6$ and 15 : 00–03 : 00 MLT.

i	0	1	2	3
	3.455e+00	9.938e+00	2.147e+00	-4.175e-01

Table 37: Values of the coefficients a_{ij} for the model of the obliquity parameter B_w in λ - K_P domain for region $2 < L < 6$ and 03 : 00–15 : 00 MLT.

i/j	0	1	2	3
0	3.404e-03	-2.598e-03	6.632e-04	-5.602e-05
1	-2.516e-03	2.291e-03	-7.378e-04	7.973e-05
2	3.950e-03	-2.701e-03	6.840e-04	-6.217e-05
3	-4.024e-04	1.374e-04	-1.248e-05	1.446e-07

Table 38: Values of the coefficients b_k for the model of the obliquity parameter of hiss waves B_w in λ - K_P domain for region $2 < L < 6$ and 03 : 00–15 : 00 MLT.

i	0	1	2	3
	9.608e+00	3.694e-01	-7.021e-01	9.496e-02

Table 39: Values of the coefficients a_{ij} for the model of the obliquity parameter of hiss waves B_w in λ - K_P domain for region $2 < L < 6$ and 15 : 00–03 : 00 MLT.

i/j	0	1	2	3
0	3.096e-03	-1.912e-03	3.750e-04	-2.054e-05
1	2.092e-03	-2.845e-03	1.090e-03	-1.278e-04
2	-1.364e-03	2.358e-03	-1.020e-03	1.329e-04
3	1.964e-03	-1.573e-03	4.667e-04	-5.097e-05

Table 40: Values of the coefficients b_k for the model of the obliquity parameter of hiss waves B_w in λ - K_P domain for region $2 < L < 6$ and 15 : 00–03 : 00 MLT.

i	0	1	2	3
	6.361e+00	-2.033e+00	8.849e-01	-6.139e-02

Table 41: Values of the coefficients a_{ij} for the model of RMS wave amplitudes of LBC waves B_w in λ - K_P domain for region $2 < L < 6$ and 3 : 00–15 : 00 MLT.

i/j	0	1	2	3
0	-5.387e-03	7.326e-03	-2.976e-03	4.128e-04
1	8.242e-02	-8.720e-02	2.861e-02	-2.777e-03
2	-1.302e-01	1.309e-01	-4.070e-02	3.759e-03
3	5.032e-02	-4.968e-02	1.519e-02	-1.389e-03

Table 42: Values of the coefficients b_k for the model of RMS wave amplitudes of LBC waves B_w in λ - K_P domain for region $2 < L < 6$ and 3 : 00–15 : 00 MLT.

i	0	1	2	3
	8.408e-01	-2.484e-01	5.387e-01	-6.574e-02

Table 43: Values of the coefficients a_{ij} for the model of RMS wave amplitudes of LBC waves B_w in λ - K_P domain for region $2 < L < 6$ and 15 : 00–3 : 00 MLT.

i/j	0	1	2	3
0	8.671e-03	-8.872e-03	2.848e-03	-2.689e-04
1	3.613e-03	-5.749e-03	2.599e-03	-3.138e-04
2	-1.691e-02	2.035e-02	-7.574e-03	8.172e-04
3	6.087e-03	-7.417e-03	2.781e-03	-3.013e-04

Table 44: Values of the coefficients b_k for the model of RMS wave amplitudes of LBC waves B_w in λ - K_P domain for region $2 < L < 6$ and 15 : 00–3 : 00 MLT.

i	0	1	2	3
	3.684e+00	-2.460e+00	2.828e+00	-3.018e-01

Table 45: Values of the coefficients a_{ij} for the model of RMS wave amplitudes of hiss waves B_w in λ - K_P domain for region $2 < L < 6$ and 3 : 00–15 : 00 MLT.

i/j	0	1	2	3
0	-1.845e-04	2.100e-04	-5.797e-05	6.122e-06
1	-2.431e-03	2.415e-03	-7.451e-04	7.421e-05
2	3.316e-03	-3.345e-03	1.053e-03	-1.078e-04
3	-1.104e-03	1.132e-03	-3.611e-04	3.759e-05

Table 46: Values of the coefficients b_k for the model of RMS wave amplitudes of hiss waves B_w in λ - K_P domain for region $2 < L < 6$ and 3 : 00–15 : 00 MLT.

i	0	1	2	3
	6.447e+01	4.626e+00	2.019e+00	-4.042e-01

Table 47: Values of the coefficients a_{ij} for the model of RMS wave amplitudes of hiss waves B_w in λ - K_P domain for region $2 < L < 6$ and 15 : 00–3 : 00 MLT.

i/j	0	1	2	3
0	3.562e-04	-1.255e-04	1.039e-05	5.484e-06
1	1.844e-03	-2.415e-03	9.311e-04	-1.108e-04
2	-4.081e-03	4.866e-03	-1.764e-03	1.990e-04
3	1.423e-03	-1.755e-03	6.523e-04	-7.461e-05

Table 48: Values of the coefficients b_k for the model of RMS wave amplitudes B_w in λ - K_P domain for region $2 < L < 6$ and 15 : 00–3 : 00 MLT.

i	0	1	2	3
	1.321e+01	9.943e+00	-1.849e+00	1.062e-01

E Examples

E.1 Python

```

import numpy as np

def get_magnetic_amplitude(coefficients, control_param1, control_param2):
    """Returns RMS value of the magnetic field amplitude
    Parameters:
    coefficients -- two-dimensional array that contains
    model coefficients;
    control_param1 -- first control parameter;
    control_param2 -- second control parameter."""
    acc = 0
    for i in xrange(0, 4):
        for j in xrange(0, 4):
            acc += a[i, j] * control_param1 ** i * control_param2 ** j

    amplitude = 10 ** acc
    return amplitude

def load_coefficients(filename):
    """Reads model coefficients from ASCII file
    and returns as two-dimensional array
    Parameters:
    filename -- full filename of the ASCII file."""
    coefficients = np.loadtxt(filename)
    return coefficients

```

E.2 MATLAB

```

function coefficients = load_coefficients(filename)
    delimiterIn = '_';
    headerlinesIn = 3;
    data = importdata(filename, delimiterIn, headerlinesIn);
    coefficients = data.data;
end

function amplitude = get_amplitude(coefs, control_param1, control_param2)
    acc = 0;
    for i = 1:4
        for j = 1:4
            acc += a(i, j) * control_param1 ^ (i-1) * control_param2 ^ (j-1);
        end
    end
    amplitude = 10 ^ acc

```

end